



Supplementary Materials for

In situ photocatalytically enhanced thermogalvanic cells for electricity and hydrogen production

Yijin Wang *et al.*

Corresponding author: Xuanhua Li, lixh32@nwpu.edu.cn

Science **381**, 291 (2023)
DOI: 10.1126/science.adg0164

The PDF file includes:

Materials and Methods
Supplementary Text
Figs. S1 to S24
Notes S1 to S3
Tables S1 to S4
References

Other Supplementary Material for this manuscript includes the following:

Movie S1

Methods

Synthesis of the polyacrylic acid-FeCN^{4-/3-} system (PAA-FeCN^{4-/3-})

0.33 mL of the 0.34 M/0.26 M FeCN⁴⁻/FeCN³⁻ electrolyte solution [containing 0.042 g potassium hexacyanoferrate (FeCN⁴⁻) and 0.028 g potassium ferricyanide (FeCN³⁻) in 0.33 mL deionized water], 0.14 g acrylic acid (AA), and 1 g 2-Hydroxyethyl methacrylate (HEMA) were mixed to form a homogeneous solution, followed by the addition of 11.1 mg ethylene glycol dimethacrylate (EDGMA), 0.1 mL (5 wt%) ammonium persulfate (APS) solution, and 0.1 mL N,N,N',N'-Tetramethylethylenediamine (TMEDAS). The mixture was stirred for 10 min and quickly transferred into cylinder-shaped molds (diameter: 20 mm, height: 9 mm). The polymerization was conducted at 323 K for 3 h.

Synthesis of the sulfur-vacancies ZnIn₂S₄ (S_v-ZIS)

The fabrication of S_v-ZIS is described in our previous work (25). Zn(NO₃)₂·4H₂O (0.5 mmol), In(NO₃)₃ (1 mmol), and thioacetamide (TAA, 2 mmol) were dissolved in 30 mL deionized water with a molar ratio of 1:2:4. Then, the mixture was sealed into a 50 mL Teflon-lined autoclave and maintained at 453 K for 24 h. Finally, S_v-ZIS was obtained by washing three times with ethanol and deionized water separately and drying at 333 K for 24 h. ZnIn₂S₄ (ZIS) was prepared using the same procedure except for the addition of 2 mmol TAA. A Pt cocatalyst was deposited on the S_v-ZIS via a reduction method. Briefly, 50 mg of S_v-ZIS was suspended in 50 mL of H₂PtCl₆ solution (Pt content = 5 mg mL⁻¹), followed by the addition of 3 mL NaBH₄ aqueous solution (containing 95 mg NaBH₄) under vigorous stirring for 3 h. Pt-immobilized S_v-ZIS precipitates (1 wt%) were collected and thoroughly washed with water and ethanol and dried at 333 K for 12 h.

Synthesis of the oxygen vacancies in WO₃ (O_v-WO₃)

The fabrication of O_v-WO₃ has been previously reported by us (25). A mixture of sodium tungstate (1 mmol) and citric acids (1.5 mmol) was added to a solution of distilled water (15 mL) and ethanol (5 mL) under vigorous stirring for 10 min. After adding 2 mL 3 M HCl and stirring for another 10 min, the solution was transferred into a 50 mL Teflon-lined autoclave and heated at 453 K for 6 h. The obtained yellow WO₃ precipitate was washed three times with deionized water and dried at 333 K. The O_v-WO₃ was obtained by annealing WO₃ powder at 773 K under an Ar atmosphere for 2 h with a heating rate of 2 K min⁻¹. CoO_x as a cocatalyst (2 wt%) was loaded on the O_v-WO₃ by impregnation from an aqueous

$\text{Co}(\text{NO}_3)_2 \cdot 6\text{H}_2\text{O}$ solution (1 g L^{-1}) and stirred for 3 h at 373 K followed by heating at 673 K for 2 h under an Ar atmosphere to form $\text{CoO}_x/\text{O}_v\text{-WO}_3$.

Synthesis of the ZrO_2/TaON (ZTO)

ZTO was fabricated according to previous work (24). $\text{ZrO}(\text{NO}_3)_2 \cdot 2\text{H}_2\text{O}$ and Ta_2O_5 were thoroughly mixed with a small amount of methanol and thermally treated at 343 K for 1 h. The resultant powder was then calcined in an Al_2O_3 crucible for 2 h at 1073 K. Finally, the $\text{ZrO}_2/\text{Ta}_2\text{O}_5$ composite was nitrogenized under an ammonia flow (20 mL min^{-1}) at 1123 K for 15 h to produce ZTO.

Synthesis of the BiVO_4 (BVO)

BVO was synthesized according to previous work (24). Normally, 60 mL of 2.0 M nitric acid solution was used to dissolve NH_4VO_3 (10 mmol) and $\text{Bi}(\text{NO}_3)_3 \cdot 5\text{H}_2\text{O}$ (10 mmol). The pH of the solution was then drastically reduced to 0.5 by adding ammonia solution (27 wt%) while stirring the mixture until a light-yellow precipitate was formed. The yellow precipitate was transferred to a 100 mL Teflon-lined stainless-steel autoclave and hydrothermally treated at 473 K for 10 h followed by 2 h of aging. An *in situ* photodeposition method was adopted to deposit of CoO_x cocatalyst on the surface of the BVO. 0.2 g BVO powder was dispersed in deionized water containing CoSO_4 (2.0 wt%). After that, the suspension was exposed to full-spectrum illumination for 2 h using a 300 W Xe lamp. After filtration, washing, and drying, the as-obtained powder CoO_x/BVO was acquired.

Synthesis of the $\text{SrTiO}_3\text{:Rh}$ (STO)

STO was synthesized according to the previous work (43). Sr, Ti, and Rh had an atomic ratio of 1.07/0.99/0.01 in SrTiO_3 . In a 10 vol% aqueous methanol solution containing $\text{RuCl}_3 \cdot n\text{H}_2\text{O}$, a Ru (0.5 wt%) cocatalyst for the H_2 evolution photocatalysts was added by a photodeposition process. The resultant powders were dried at 343 K for 2 h after being washed with distilled water.

Synthesis of the Cs/WO_3 (CWO)

CWO was synthesized according to the previous work (43). The WO_3 powder was first thermally treated in the air for 2 h at 973 K to increase crystallinity. An ultrasonic bath was used to sonicate the powder (10 g) in water (500 mL) for 15 min, and then, small particles that did not precipitate were removed by decantation. The acquired powder dried at 343 K for 2 h. An impregnation procedure was used to modify the surface. The WO_3 powder (1.0 g) was dissolved in 0.63 mL of a 110 mM CsCl

solution, which was then raised the pH to 1 using an HCl solution. The slurry was then evaporated to dryness before being subjected to a 30 min heat treatment at 773 K. To allow for ion exchange, the powder was agitated for 15 min in a 50 mL aqueous solution containing 50 mM FeSO₄ and 1 M H₂SO₄.

Synthesis of O_v-WO₃/PAA-FeCN^{4-/3-}/S_v-ZIS

In this process, photocatalysts such as S_v-ZIS powder (2.5 mg) and O_v-WO₃ powder (3 mg) were dispersed separately in 0.11 mL of the 0.34 M/0.26 M FeCN⁴⁻/FeCN³⁻ electrolyte by ultrasonication and stirring for 30 min, followed by the addition of corresponding proportions of AA, HEMA, DGMA, APS, and TMEDA. And then, the mixed solution was transferred into cylinder-shaped molds and heated at 323 K for 10 min, followed by the addition of corresponding PAA-FeCN^{4-/3-}/S_v-ZIS, PAA-FeCN^{4-/3-}, and O_v-WO₃/PAA-FeCN^{4-/3-}. Finally, the O_v-WO₃/PAA-FeCN^{4-/3-}/S_v-ZIS sample was acquired. The preparation of the other samples loaded with different photocatalysts was similar to that of O_v-WO₃/PAA-FeCN^{4-/3-}/S_v-ZIS.

Characterization of the samples

Voltage-time and current-voltage curves were obtained with a Keithley 2450 instrument. Then, the power-voltage curves were calculated by the corresponding current and voltage values. The corresponding temperature was acquired by an infrared camera (UTi80). The ionic concentrations were detected by ultraviolet-visible (UV-vis) spectra with a UV-2600 spectrophotometer. The ultraviolet-visible diffuse reflectance spectroscopy (UV-vis DRS) was performed with a UV-2600 spectrophotometer by a diffuse reflectance method with BaSO₄ as the reference. Cyclic voltammetry (CV) measurement scanned from - 1 V to + 1 V on the electrochemical workstation (CHI760). The scanning electron microscopy (SEM) images and energy dispersive X-ray spectroscopy (EDX) were collected on the SEM (FEI Helios G4 CX 450) equipped with an EDX spectrometer. The sample's morphology was recorded on transmission electron microscopy (TEM) (FEI Talos F200X), which was equipped with EDX spectroscopy. X-ray photoelectron spectroscopy (XPS) and ultraviolet photoelectron spectra (UPS) measurements were detected by using a Kratos spectrometer (Axis Supra) with a monochromatic Al K α source. Electron spin resonance (ESR) spectra were measured on a Bruker EMXmicro-6/1/P/L spectrometer at 300 K and 9.062 GHz. Raman and *in situ* Raman spectra were recorded on a Renishaw RM1000 laser Raman spectrometer using a laser excitation of 532 nm, equipped with a Xe lamp. The X-ray diffraction (XRD) (BRUKER D2 PHASER) using Cu K α

($\lambda=1.5406 \text{ \AA}$) radiation was used to assess the crystalline structure of the as-synthesized samples. The thermal conductivity (κ) of the samples was measured by the Hot Disk. The electrical conductivity of the samples was acquired from the slope of the current-voltage curve via a Keithley 2450 sourcemeter.

Overall photocatalytic water-splitting reaction

Photocatalytic reactions were carried out in a reaction vessel that was connected to a condensate system with a temperature of 298.5 K. The photocatalytically enhanced thermogalvanic system was immersed in 2 mL of water. Prior to each reaction, the equipment was thoroughly degassed under vacuum. A solar simulator operating at 1.5G illumination (100 mW cm^{-2}) (CEL-NP2000, Beijing China Education Au-light Technology Co., Ltd.) was used as the light source to trigger the photocatalytic generation of H_2 and O_2 . Moreover, the amounts of H_2 and O_2 evolution were monitored by online gas chromatography (Shimadzu GC-2014C, molecular sieve-5A, and Ar as the carrier gas).

Step-by-step fabrication of a large area of photocatalytically enhanced thermogalvanic device

We first prepared a reaction module (90 mm×90 mm) made of polymethyl methacrylate (PMMA) with 9 units. Every unit is a cylinder-shaped mold (diameter: 20 mm, height: 9 mm). Nine photocatalytically enhanced thermogalvanic systems were connected in series via copper wires. Finally, the isolated four PMMA reaction modules were connected in series to construct a 36-unit large-area system. Furthermore, we also attached a gas collection bag to the PMMA reaction cell to collect the hydrogen and oxygen produced by the overall photocatalytic water splitting.

Calculation of the thermopower

The open-circuit voltage was recorded using Keithley 2450 instrument. Au@Cu (10 μm thickness) mesh and Au@Cu foil (10 μm thickness) were used as the hot and cold electrodes, respectively. To create Au@Cu electrodes, Au (100 nm) was thermally evaporated on the Cu mesh or Cu foil (2×10^{-6} mbar) by the Braun steaming equipment. The temperatures were recorded by an infrared camera (UTi80). The thermopower was calculated according to Eq. 1 (41):

$$S_e = -\frac{E_{\text{hot}} - E_{\text{cold}}}{T_{\text{hot}} - T_{\text{cold}}} \quad (1)$$

where S_e is the thermopower, E_{hot} and E_{cold} is the potential at the hot and cold sides of the sample, respectively. T_{hot} and T_{cold} are the temperature at the hot and cold sides of the sample, respectively.

Calculation of the normalized output power density ($P_{\max}/\Delta T^2$)

For the normalized maximum power density tests, the distance between the two electrodes was 0.9 cm, and the cross-sectional area of the thermogalvanic cell was 3.14 cm². The current-voltage curves were measured from 0 V to the open-circuit voltage. The power-voltage curves were calculated according to Eq. 2 (18):

$$P_{\max} = \frac{V_{\text{oc}} I_{\text{sc}}}{4} \quad (2)$$

where V_{oc} and I_{sc} are the open-circuit voltage and short-circuit current, respectively.

Calculation of Carnot-relative efficiency (η_r) and figure of merit (ZT)

The energy conversion efficiency (η) of a thermoelectric device is defined as the ratio of the maximum electrical output power (P_{\max}) from the thermogalvanic cell to the heat input power (P_{heat}) (1).

$$\eta = \frac{P_{\max}}{P_{\text{heat}}} = \frac{P_{\max} d}{\kappa \Delta T} \quad (3)$$

where d , ΔT , and κ are the thickness, temperature difference between hot and cold electrodes, and thermal conductivity, respectively. The value of d used for the calculations was 0.9 cm. ΔT was 16.8 K, and κ was 0.50 W m⁻¹ K⁻¹. The detailed temperature is shown in **Fig. S8**, and the detailed κ is presented in **Fig. S16B**.

The Carnot-relative efficiency (η_r) is calculated by (1):

$$\eta_r = \frac{\eta}{\Delta T / T_{\text{hot}}} = \frac{P_{\max} d T_{\text{hot}}}{\kappa \Delta T^2} \quad (4)$$

where T_{hot} is the temperature at the hot side of the sample. The value of T_{hot} was 315.4 K.

The performance of thermogalvanic cells is typically evaluated using the figure-of-merit ($ZT = \frac{S_e^2 \sigma}{\kappa}$). However, this definition is not directly applicable to the cells with thermodiffusion effects due to their transient behavior. In the current work, we observed that the thermodiffusion effect has a minor impact on the thermopower. Therefore, we amended the calculation of the ZT by subtracting the thermodiffusion contribution factor, which is often calculated according to Eq. 5 (41):

$$ZT = \frac{(S_e - S_{\Delta D})^2 \sigma}{\kappa} T \quad (5)$$

where S_e is the thermopower driven by both thermodiffusion and thermogalvanic effects. $S_{\Delta D}$ is the thermopower caused only by the thermodiffusion effect. σ and κ are electrical conductivity and thermal conductivity obtained at absolute temperature (T), respectively. σ was 4.7 S m⁻¹ (calculated from the

I-V curve in **Fig. S16A**). κ was $0.50 \text{ W m}^{-1} \text{ K}^{-1}$. T was 307 K (the average between cold and hot side temperatures).

Calculation of the solar to hydrogen (STH) energy conversion efficiency

The STH efficiency was determined according to the following Eq. 6 (44):

$$\text{STH}(\%) = \frac{R_{\text{H}_2} \Delta G_r}{PS} \times 100 \quad (6)$$

here, R_{H_2} , ΔG_r , P , and S denote the H_2 evolution rate during the overall water-splitting reaction, the Gibbs energy for the water-splitting reaction, the light energy flux of the AM 1.5 solar irradiation, and the irradiated sample area, respectively. ΔG_r was 237 kJ mol^{-1} . P was 100 mW cm^{-2} . S was 0.64 cm^2 .

Theoretical calculation of photocatalysts with the electric field

Density Functional Theory (DFT) calculations were performed by using the Vienna *Ab initio* Simulation Package (VASP) (45). The projector augmented wave (PAW) pseudopotential and the Perdew–Burke–Ernzerhof (PBE) exchange-correlation functional within a generalized gradient approximation (GGA) were adopted (46). The K-point was set as $3 \times 3 \times 1$ and the plane wave energy cutoff was 500 eV (47). The convergence tolerance of electronic energy was set to 10^{-5} eV, and forces were converged to within 0.02 eV/\AA . The van der Waals interactions were considered by using the Grimme method (DFT-D3) (48). The VASP implicit solvent model was used to evaluate the effect of water (49). The computational hydrogen electrode (CHE) model was used to calculate the Gibbs free energy G (50), which was defined as:

$$G = E + \text{ZPE} + \int C_p dT - TS \quad (7)$$

where E is the electron energy obtained by DFT calculations, ZPE , $\int C_p dT$, and TS are the zero-point energy, enthalpy change, and entropy correction at room temperature ($T = 298.15 \text{ K}$).

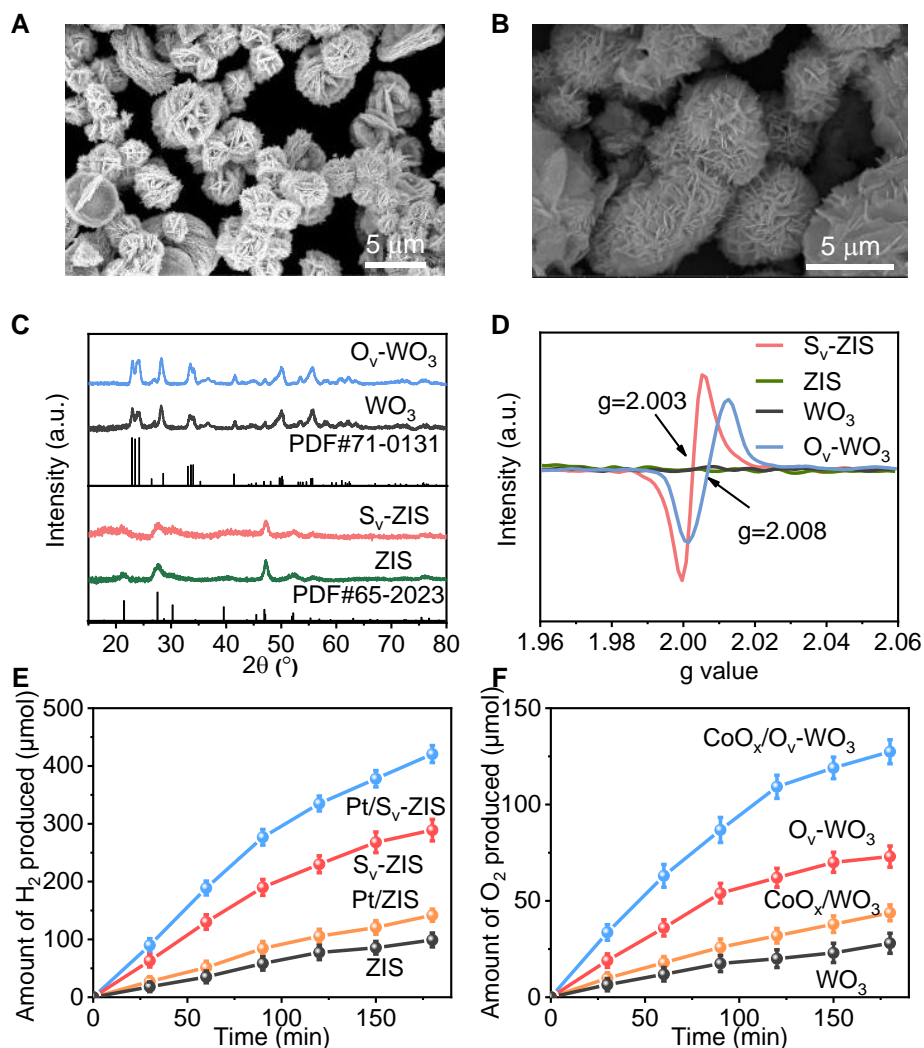


Fig. S1. The morphology, structure, and photocatalytic performance of S_v -ZIS and O_v - WO_3 . SEM images of (A) WO_3 and (B) ZIS. (C) XRD patterns and (D) ESR profiles of WO_3 , O_v - WO_3 , ZIS, and S_v -ZIS. (E) Photocatalytic H_2 evolution over ZIS, S_v -ZIS, Pt/ZIS and Pt/ S_v -ZIS under the 100 mW cm^{-2} light irradiation in the presence of $FeCN^{4-}$ (0.3 mol L^{-1}) as hole scavenger (Reaction conditions: 20 mg photocatalyst; 10 mL $FeCN^{4-}$ solution). (F) Photocatalytic O_2 evolution of WO_3 , O_v - WO_3 , CoO_x/WO_3 , and CoO_x/O_v - WO_3 under the 100 mW cm^{-2} light irradiation in the presence of $FeCN^{3-}$ (0.3 mol L^{-1}) as electron scavenger (Reaction conditions: 20 mg photocatalyst; 10 mL $FeCN^{3-}$ solution). Error bars denoted the standard deviation from three times repeated measurements. Pristine WO_3 and ZIS showed no apparent peaks in the ESR surveys. A strong signal at $g = 2.003$ was acquired from S_v -ZIS, which arises from the S vacancies. Meanwhile, the signal at $g = 2.008$ was attributed to O vacancies in the O_v - WO_3 (Fig. S1D) (51, 52).

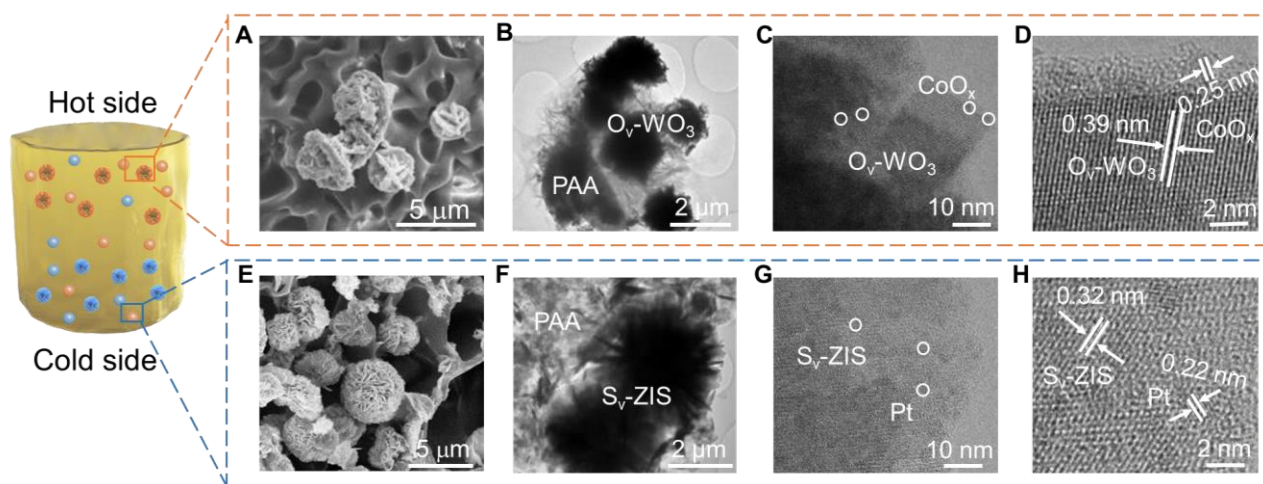


Fig. S2. The morphology of $\text{O}_v\text{-WO}_3/\text{TGC}/\text{S}_v\text{-ZIS}$ system. (A) SEM image, (B and C) Low-magnification TEM images, (D) HRTEM image of $\text{O}_v\text{-WO}_3/\text{TGC}$. (E) SEM image, (F and G) Low-magnification TEM images, and (H) HRTEM image of $\text{TGC}/\text{S}_v\text{-ZIS}$.

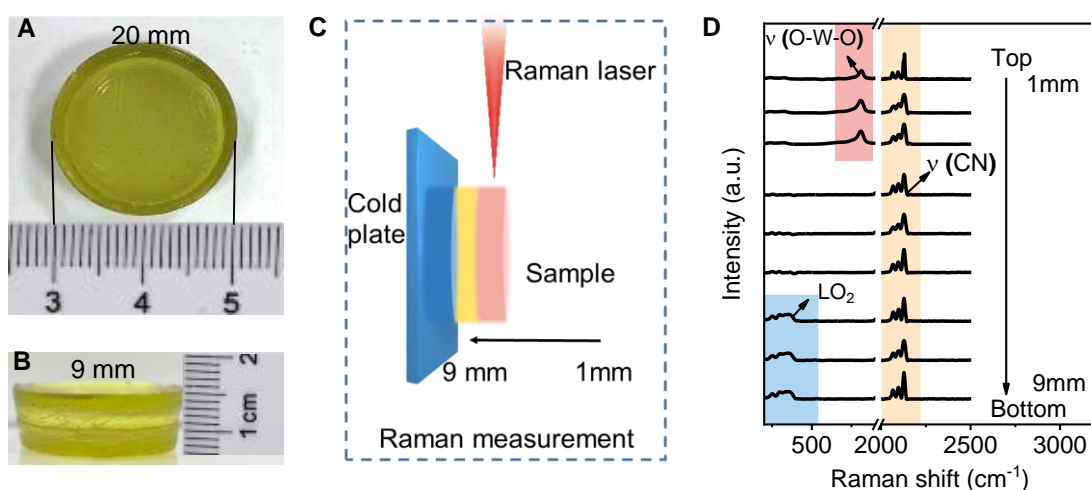


Fig. S3. The depth distribution of catalysts by Raman analysis in the $O_v\text{-WO}_3/\text{TGC}/S_v\text{-ZIS}$ system. (A) Top and (B) side-view digital images of the $O_v\text{-WO}_3/\text{TGC}/S_v\text{-ZIS}$. (C) Schematic of the system with the Raman measurement at different depths. (D) Raman spectra were measured along the vertical section of $O_v\text{-WO}_3/\text{TGC}/S_v\text{-ZIS}$ at different depths. Peaks at 813 nm and 359 nm corresponded to the $\nu_{(O-W-O)}$ characteristic peak of $O_v\text{-WO}_3$ and the LO_2 peak of $S_v\text{-ZIS}$, respectively. $\nu_{(\text{CN})}$ characteristic peaks of $\text{FeCN}^{4-/3-}$ were observed at 2058, 2091, and 2128 nm (**Fig. S3D**).

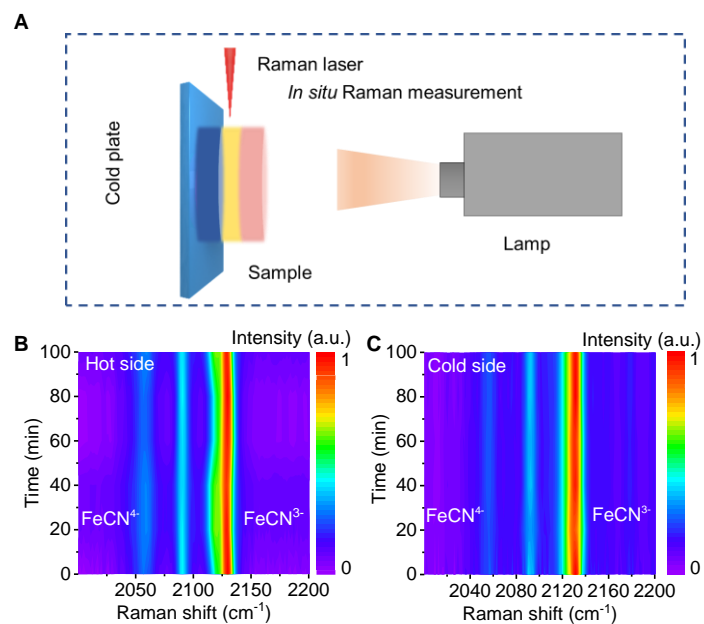


Fig. S4. In situ Raman analysis to monitor real-time concentration changes of $\text{FeCN}^{3-}/\text{FeCN}^{4-}$ in the system. (A) Schematic of in situ Raman analysis to monitor real-time concentration changes of FeCN^{3-} and FeCN^{4-} in the system under light irradiation. Real-time $\text{FeCN}^{4-/3-}$ monitoring through in situ Raman analysis for the (B) hot and (C) cold sides of TGC under the light irradiation.

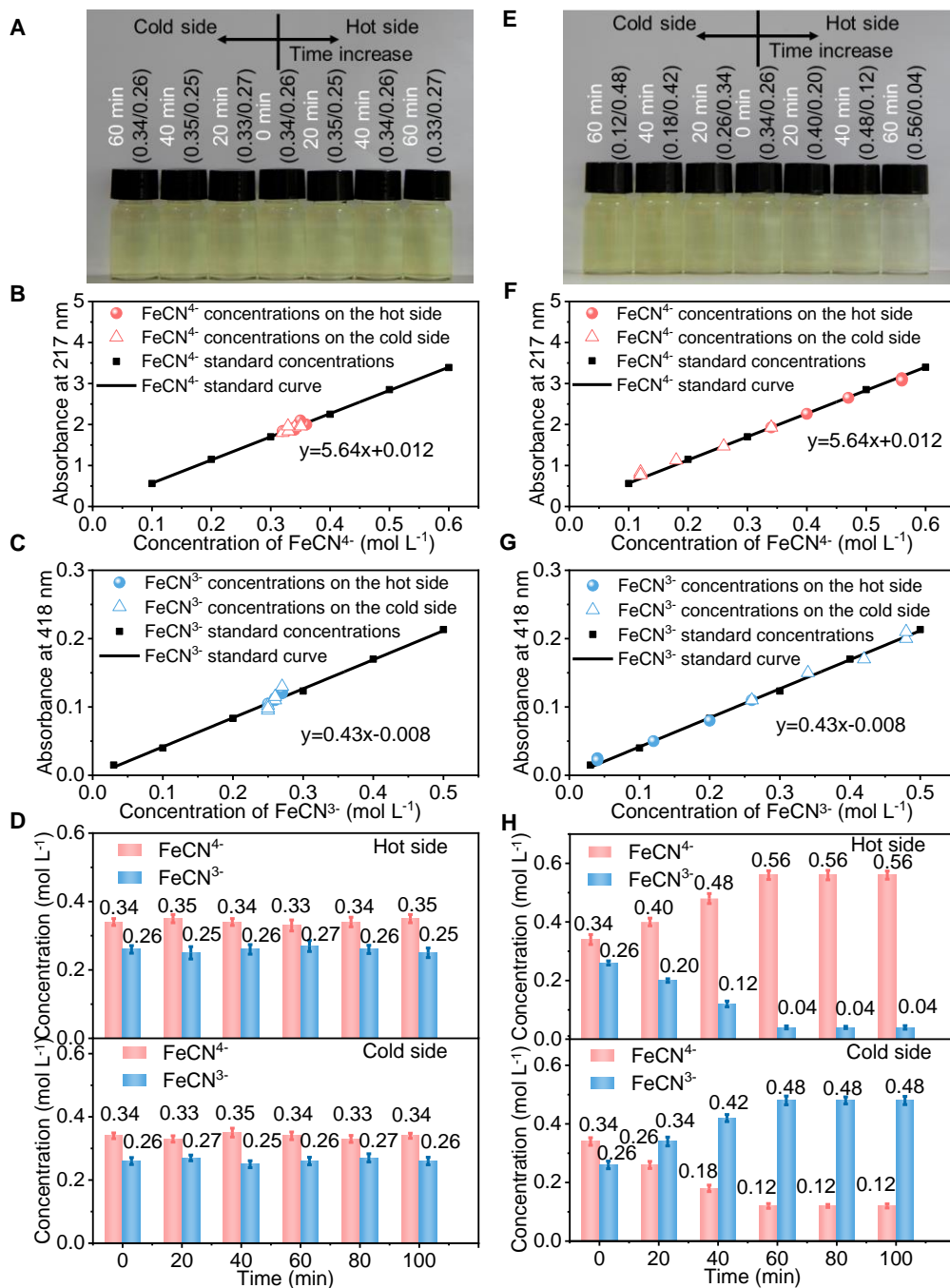


Fig. S5. UV-vis absorption measurement for the FeCN⁴⁻/FeCN³⁻ concentration in the system. (A) Digital image and (B to D) time courses of concentrations for FeCN⁴⁻ and FeCN³⁻ on the hot and cold sides of the TGC system under light irradiation. (E) Digital image and (F to H) time courses of concentrations for FeCN⁴⁻ and FeCN³⁻ on the hot and cold sides of the O_v-WO₃/TGC/S_v-ZIS system under light irradiation. Error bars denoted the standard deviation from ten times repeated measurements. Based on the Lambert-Beer law of UV-vis absorption spectra, FeCN³⁻ and FeCN⁴⁻ concentrations were quantitatively analyzed (53). The FeCN⁴⁻ and FeCN³⁻ concentrations on the cold and hot sides were determined through UV-vis absorption spectra using the standard curve method. During the light irradiation, we extracted 0.05 g of the sample on the hot and cold sides of the system for 20 min intervals and soaked it in 3 mL of deionized water for 20 h. Thus, we acquired the test-related solution.

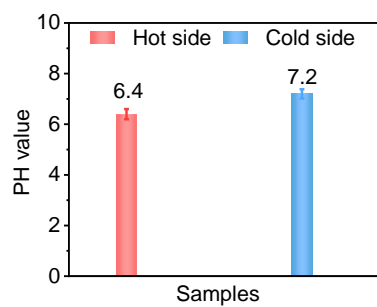


Fig. S6. PH values on both sides of O_v-WO₃/TGC/S_v-ZIS under light irradiation after 60 min. Error bars indicated the standard deviation for three measurements. The pH values on the hot and cold side after 60 min of the light irradiation were 6.4 (H⁺ concentration: 3.9×10⁻⁷ mol L⁻¹) and 7.2 (H⁺ concentration: 0.6×10⁻⁷ mol L⁻¹), respectively. Therefore, the concentration difference of H⁺ between the hot and cold side was 3.3×10⁻⁷ mol L⁻¹.

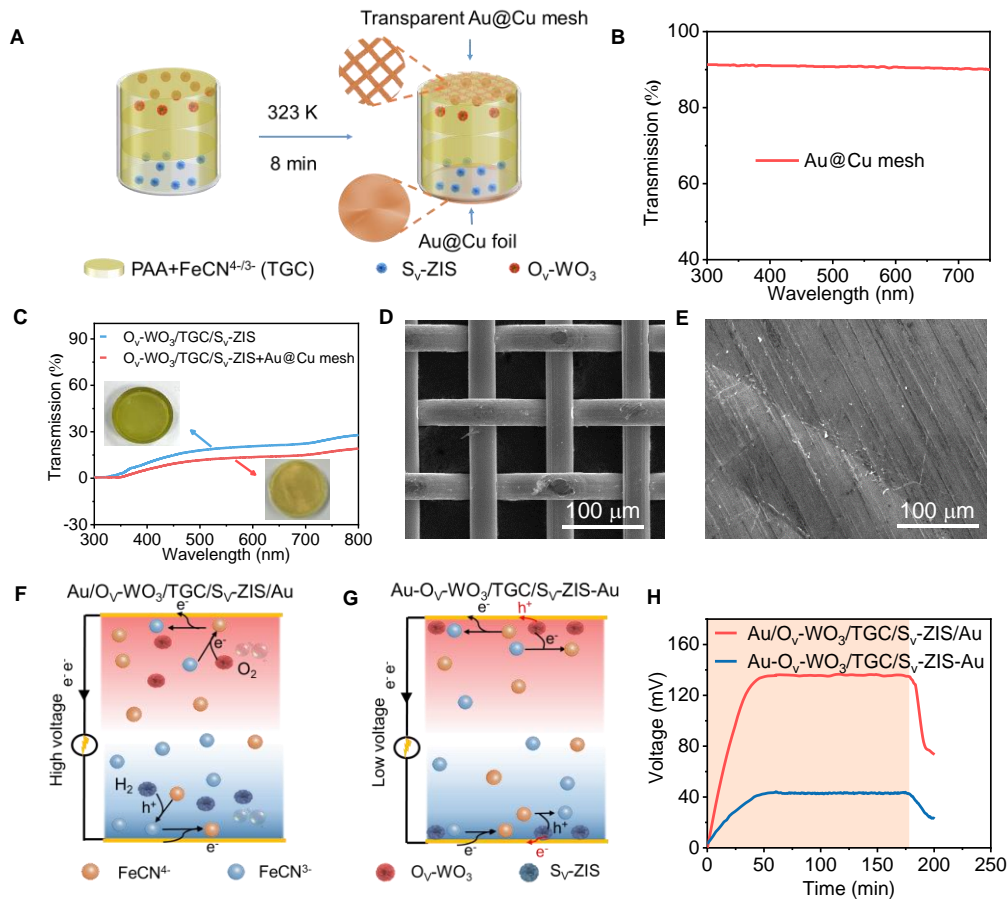


Fig. S7. The characterization of electrodes. (A) Schematic illustration of the Au@Cu mesh+O_v-WO₃/TGC/S_v-ZIS+Au@Cu foil fabrication. (B) Transmission spectrum of Au@Cu mesh. (C) Transmission spectra of O_v-WO₃/TGC/S_v-ZIS and O_v-WO₃/TGC/S_v-ZIS+Au@Cu mesh. (Inset: Digital images of Au@Cu mesh+O_v-WO₃/TGC/S_v-ZIS and O_v-WO₃/TGC/S_v-ZIS.) SEM images of (D) the Au@Cu mesh and (E) Au@Cu foil. Schematic diagram of electron transport for (F) Au/O_v-WO₃/TGC/S_v-ZIS/Au and (G) Au-O_v-WO₃/TGC/S_v-ZIS-Au. (H) Open-circuit voltage response versus time curves of Au/O_v-WO₃/TGC/S_v-ZIS/Au and Au-O_v-WO₃/TGC/S_v-ZIS-Au. We choose Cu electrodes due to their inexpensiveness. The Cu electrodes were coated with Au particles to avoid electrode corrosion of the O_v-WO₃/TGC/S_v-ZIS (7). O_v-WO₃ and S_v-ZIS were loaded within the PAA matrix and did not contact the electrodes directly. A transparent hot electrode, consisting of an Au-coated Cu (Au@Cu) mesh with 91% transmittance, was utilized by pressing it against the PAA hydrogel and securing it with transparent conductive adhesives surrounding the edge. Meanwhile, an Au@Cu foil was employed as the cold electrode and sealed with transparent epoxy. Compared with the catalyst directly attached to the electrode (Au-O_v-WO₃/TGC/S_v-ZIS-Au), the presence of O_v-WO₃ and S_v-ZIS in the PAA matrix (Au/O_v-WO₃/TGC/S_v-ZIS/Au) was more conducive to the reaction between the catalyst and FeCN^{3-/4-}, improving the concentration gradient. Consequently, the open-circuit voltage of the Au/O_v-WO₃/TGC/S_v-ZIS/Au reached 137 mV. For the Au-O_v-WO₃/TGC/S_v-ZIS-Au system, under light illumination, the photogenerated holes of O_v-WO₃ and the photogenerated electrons of S_v-ZIS were transferred to the electrode. The electrons flowed in the opposite direction of the thermogalvanic cells of FeCN^{4-/3-}. As a result, the voltage of the Au-O_v-WO₃/TGC/S_v-ZIS-Au system decreased to 42 mV (Figs. S7F to H).

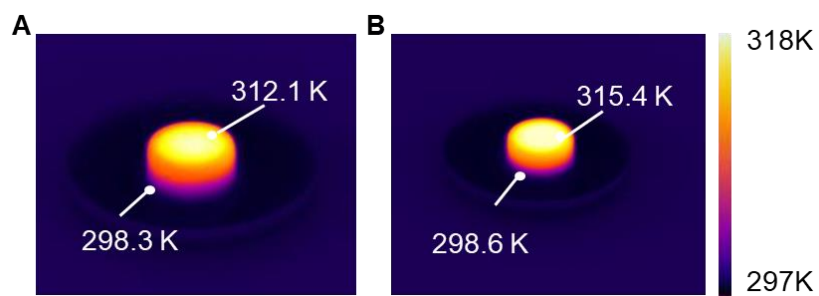


Fig. S8. Infrared thermal images. (A) TGC and (B) $O_v\text{-WO}_3/\text{TGC}/S_v\text{-ZIS}$ with the electrodes.

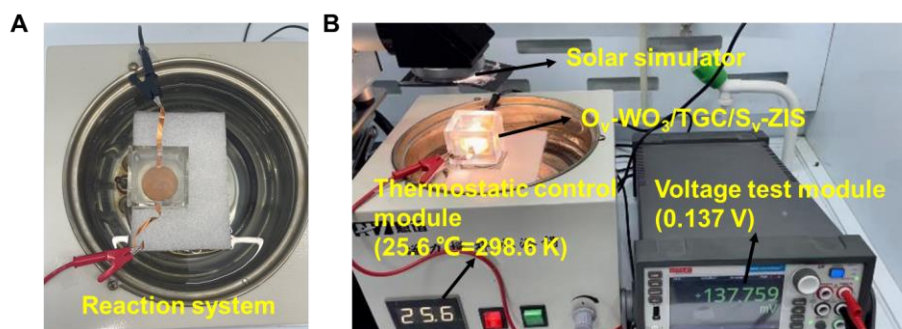


Fig. S9. Real pictures of the cells. (A) Reaction system, and (B) measurement setup for photocatalytically enhanced thermogalvanic cells. The temperature (298.6 K) and the voltage (0.137 V) were in **Fig. 1F** and **Fig. 2B** of the main text, respectively.

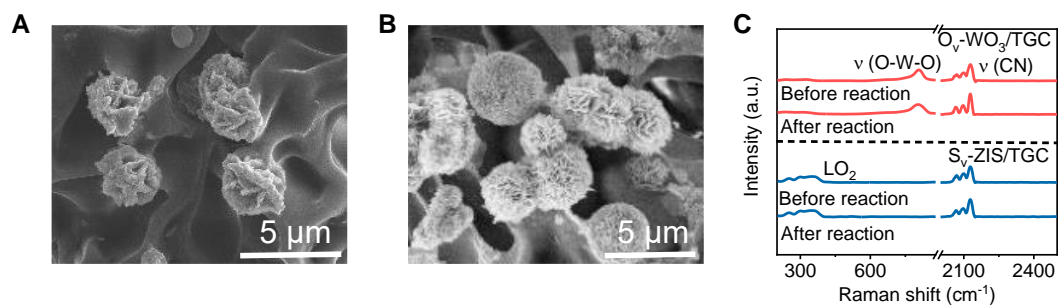


Fig. S10. The characterization of $O_v\text{-WO}_3/\text{TGC}/S_v\text{-ZIS}$ after the photocatalytic reaction. SEM images of (A) $O_v\text{-WO}_3/\text{TGC}$ and (B) $\text{TGC}/S_v\text{-ZIS}$. (C) Raman spectra of $O_v\text{-WO}_3/\text{TGC}$ and $\text{TGC}/S_v\text{-ZIS}$ before and after the photocatalytic reaction.

Note S1. The weight coefficient of ΔD , ΔS and ΔC in the $O_v\text{-WO}_3/\text{TGC}/S_v\text{-ZIS}$ system

The mechanism of enhanced ΔS between FeCN^{4-} and FeCN^{3-} : We explored the reason for the enhanced ΔS of FeCN^{4-} and FeCN^{3-} in the $O_v\text{-WO}_3/\text{TGC}/S_v\text{-ZIS}$ system. ΔS arises from the interactions between the redox ions and monomer units of PAA (19). The intermolecular interaction is usually evaluated using UV-vis absorption spectroscopy and XPS spectroscopy (2). Based on UV-vis absorption spectra analysis, we evaluated the intermolecular interaction between the $\text{FeCN}^{4-/3-}$ and monomer units [with or without photocatalysts ($O_v\text{-WO}_3/S_v\text{-ZIS}$)] in **Figs. S11A and B** (18). Acrylic acid (AA) and 2-Hydroxyethyl methacrylate (HEMA) are precursors of PAA (see details in the Methods). We observed a significant shift in the UV-vis absorbance band of FeCN^{4-} from 217 to 220 nm with the addition of HEMA and $O_v\text{-WO}_3/S_v\text{-ZIS}$ simultaneously, whereas the band location of FeCN^{4-} remained almost unchanged with the addition of AA. The UV-vis absorbance bands of FeCN^{3-} were unchanged with the addition of AA, HEMA, $O_v\text{-WO}_3/S_v\text{-ZIS}$, and $O_v\text{-WO}_3/S_v\text{-ZIS}+\text{HEMA}$, respectively. These results indicated that the HEMA units and $O_v\text{-WO}_3/S_v\text{-ZIS}$ synergistically had a stronger interaction with FeCN^{4-} , which could increase ΔS of the $\text{FeCN}^{4-/3-}$ and enhance the thermopower of thermogalvanic cells. We further investigated the interaction between thermogalvanic ions and monomer units (with or without photocatalysts) by XPS (2). The solid composite samples used for XPS measurement were prepared by drying the composite solutions in a vacuum oven at 333 K for 24 h. **Fig. S11C** showed the N1s spectra of FeCN^{4-} , $\text{FeCN}^{4-}+\text{AA}$, $\text{FeCN}^{4-}+\text{HEMA}$, $\text{FeCN}^{4-}+O_v\text{-WO}_3/S_v\text{-ZIS}$, and $\text{FeCN}^{4-}+O_v\text{-WO}_3/S_v\text{-ZIS}+\text{HEMA}$. The N1s binding energy of the mixture of $\text{FeCN}^{4-}+O_v\text{-WO}_3/S_v\text{-ZIS}+\text{HEMA}$ shifted to higher binding energy compared to the pure FeCN^{4-} sample. By contrast, the N1s binding energy of all composite samples with FeCN^{3-} only exhibited a slight shift compared to the pure FeCN^{3-} sample, respectively (**Fig. S11D**). The results observed from XPS and the UV-vis spectra revealed that HEMA units and $O_v\text{-WO}_3/S_v\text{-ZIS}$ synergistically had stronger interaction with FeCN^{4-} than with FeCN^{3-} .

The existence of ΔD : We used an isothermal three-electrode system to determine the temperature coefficient and the thermodiffusion thermopower. In the TGC system, the temperature coefficient of $\text{FeCN}^{4-/3-}$ was measured to be -1.7 mV K^{-1} vs the saturated calomel electrode (SCE). It was worth noting that the SCE itself had a temperature coefficient of -0.5 mV K^{-1} , resulting in a temperature coefficient of $\text{FeCN}^{4-/3-}$ of -2.2 mV K^{-1} (**Fig. S11E**), which was opposite to the sign convention of the thermogalvanic thermopower. The total thermopower was the sum of the thermogalvanic thermopower and thermodiffusion thermopower. The total thermopower of TGC was measured to be 2.7 mV K^{-1} (**Fig. S12C**). Thus, we could derive that the thermodiffusion thermopower of ions (i.e., K^+ , $\text{FeCN}^{4-/3-}$, H^+) in TGC contributed 0.5 mV K^{-1} (i.e., $2.7 \text{ mV K}^{-1}-2.2 \text{ mV K}^{-1}$). For the $O_v\text{-WO}_3/\text{TGC}/S_v\text{-ZIS}$, the

temperature coefficient of $\text{FeCN}^{4-/3-}$ and the thermodiffusion thermopower were -2.5 mV K^{-1} (i.e., -2.0 mV K^{-1} - 0.5 mV K^{-1}) and 1 mV K^{-1} (i.e., 3.5 mV K^{-1} - 2.5 mV K^{-1}), respectively. The thermopower driven by thermodiffusion of K^+ , H^+ and $\text{FeCN}^{4-/3-}$ enhanced in the $\text{O}_v\text{-WO}_3/\text{TGC}/\text{S}_v\text{-ZIS}$ due to the more negatively charged surface of $\text{O}_v\text{-WO}_3/\text{PAA}/\text{S}_v\text{-ZIS}$ (**Fig. S11F**). Compared with the temperature coefficient in TGC, the temperature coefficient in $\text{O}_v\text{-WO}_3/\text{TGC}/\text{S}_v\text{-ZIS}$ increased due to the strong intermolecular interaction of the PAA matrix, photocatalysts, and FeCN^{4-} (**Figs. S11A-D**).

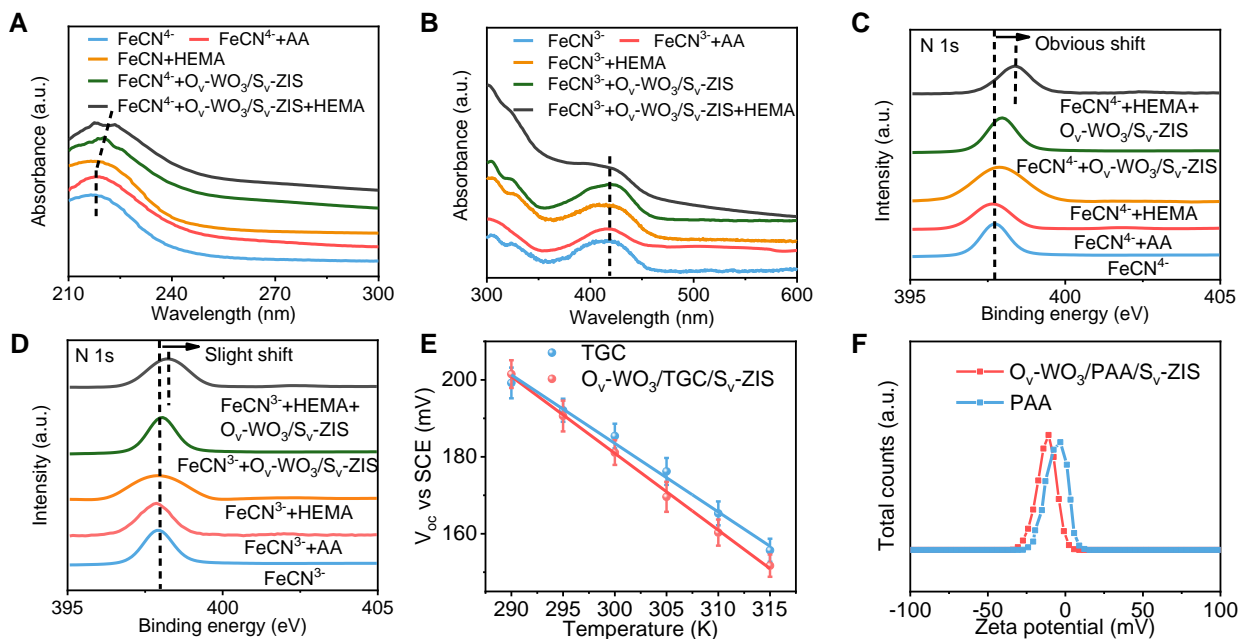


Fig. S11. The enhanced ΔD and ΔS of $\text{FeCN}^{4-/3-}$ in the $\text{O}_v\text{-WO}_3/\text{TGC}/\text{S}_v\text{-ZIS}$ system. (A) UV-vis absorption spectra of the FeCN^{4-} , $\text{FeCN}^{4-}+\text{AA}$, $\text{FeCN}^{4-}+\text{HEMA}$, $\text{FeCN}^{4-}+\text{O}_v\text{-WO}_3/\text{S}_v\text{-ZIS}$, and $\text{FeCN}^{4-}+\text{O}_v\text{-WO}_3/\text{S}_v\text{-ZIS}+\text{HEMA}$, respectively. (B) UV-vis absorption spectra of the FeCN^{3-} , $\text{FeCN}^{3-}+\text{AA}$, $\text{FeCN}^{3-}+\text{HEMA}$, $\text{FeCN}^{3-}+\text{O}_v\text{-WO}_3/\text{S}_v\text{-ZIS}$, and $\text{FeCN}^{3-}+\text{O}_v\text{-WO}_3/\text{S}_v\text{-ZIS}+\text{HEMA}$, respectively. (C) N 1s XPS spectra of the FeCN^{4-} , $\text{FeCN}^{4-}+\text{AA}$, $\text{FeCN}^{4-}+\text{HEMA}$, $\text{FeCN}^{4-}+\text{O}_v\text{-WO}_3/\text{S}_v\text{-ZIS}$, and $\text{FeCN}^{4-}+\text{O}_v\text{-WO}_3/\text{S}_v\text{-ZIS}+\text{HEMA}$, respectively. (D) N 1s XPS spectra of the FeCN^{3-} , $\text{FeCN}^{3-}+\text{AA}$, $\text{FeCN}^{3-}+\text{HEMA}$, $\text{FeCN}^{3-}+\text{O}_v\text{-WO}_3/\text{S}_v\text{-ZIS}$, and $\text{FeCN}^{3-}+\text{O}_v\text{-WO}_3/\text{S}_v\text{-ZIS}+\text{HEMA}$, respectively. (E) Open-circuit voltages at different temperatures of TGC and $\text{O}_v\text{-WO}_3/\text{TGC}/\text{S}_v\text{-ZIS}$ in an isothermal three-electrode system. Platinum served as the working electrode, while the saturated calomel electrode was used as the reference and counter electrodes. Error bars indicated the standard deviation for three measurements. (F) Zeta potential measurement of PAA and $\text{O}_v\text{-WO}_3/\text{PAA}/\text{S}_v\text{-ZIS}$.

Weight coefficient of $\Delta D+\Delta S$ and ΔC in whole system: We observed that the control TGC system without photocatalysts under light irradiation had a thermopower of only 2.7 mV K^{-1} , which was driven by ions thermodiffusion (ΔD) and entropy difference (ΔS). In contrast, the $\text{O}_v\text{-WO}_3/\text{TGC}/\text{S}_v\text{-ZIS}$ system under light irradiation had a much higher thermopower of 8.2 mV K^{-1} , which was driven by ΔD , ΔS , and ΔC (i.e., the effect of photocatalytic water splitting). To determine the weight coefficient of $\Delta D+\Delta S$ and ΔC in the $\text{O}_v\text{-WO}_3/\text{TGC}/\text{S}_v\text{-ZIS}$ system, we eliminated the ΔC caused by photocatalytic water splitting and measured the thermopower of $\text{O}_v\text{-WO}_3/\text{TGC}/\text{S}_v\text{-ZIS}$ only

driven by $\Delta D + \Delta S$ without photocatalytic reaction in **Fig. S12A**. We adopt a heating plate to replace light irradiation to eliminate the effect of ΔC . The ΔT of 16.8 K in the system was controlled by an electrical heating plate (on the top) and a water-cooled plate (on the bottom). The cold plate was held at 298.6 K, and the hot plate was controlled at 315.4 K. This ΔT was the same as the ΔT of 16.8 K in the $O_v\text{-WO}_3/\text{TGC}/S_v\text{-ZIS}$ system under light irradiation. The open-circuit voltage (V_{oc}) and thermopower of $O_v\text{-WO}_3/\text{TGC}/S_v\text{-ZIS}$ only driven by $\Delta D + \Delta S$ were 59 mV and 3.5 mV K^{-1} , respectively, which was due to ΔS and ΔD only, as the photocatalytic reaction was not applied (**Figs. S12B and C**). After the photocatalytic reaction took place, we observed an enhanced thermopower from 3.5 mV K^{-1} to 8.2 mV K^{-1} with enhanced ΔC . We decoupled the contributions of $\Delta D + \Delta S$ and ΔC caused by the photocatalysts to the thermopower values in the $O_v\text{-WO}_3/\text{TGC}/S_v\text{-ZIS}$ system (**Fig. S12D**). The relative contributions of $\Delta D + \Delta S$ and ΔC to the enhanced thermopower in $O_v\text{-WO}_3/\text{TGC}/S_v\text{-ZIS}$ under light irradiation were determined as follows: 8% contribution of $\Delta D + \Delta S$ (calculated from $\frac{S_{O_v\text{-WO}_3/\text{TGC}/S_v\text{-ZIS}(\Delta D+\Delta S)} - S_{\text{TGC}(\Delta D+\Delta S)} - S_{\Delta S}^{H^+}}{S_{O_v\text{-WO}_3/\text{TGC}/S_v\text{-ZIS}(\Delta D+\Delta S+\Delta C)} - S_{\text{TGC}(\Delta D+\Delta S)}} = \frac{3.5-2.7+0.4}{8.2-2.7} = 0.08$) and 92% contribution of ΔC (calculated from $\frac{S_{O_v\text{-WO}_3/\text{TGC}/S_v\text{-ZIS}(\Delta D+\Delta S)} - S_{\text{TGC}(\Delta D+\Delta S)} - S_{\Delta S}^{H^+}}{S_{O_v\text{-WO}_3/\text{TGC}/S_v\text{-ZIS}(\Delta D+\Delta S+\Delta C)} - S_{\text{TGC}(\Delta D+\Delta S)}} = 1 - 0.08 = 0.92$).

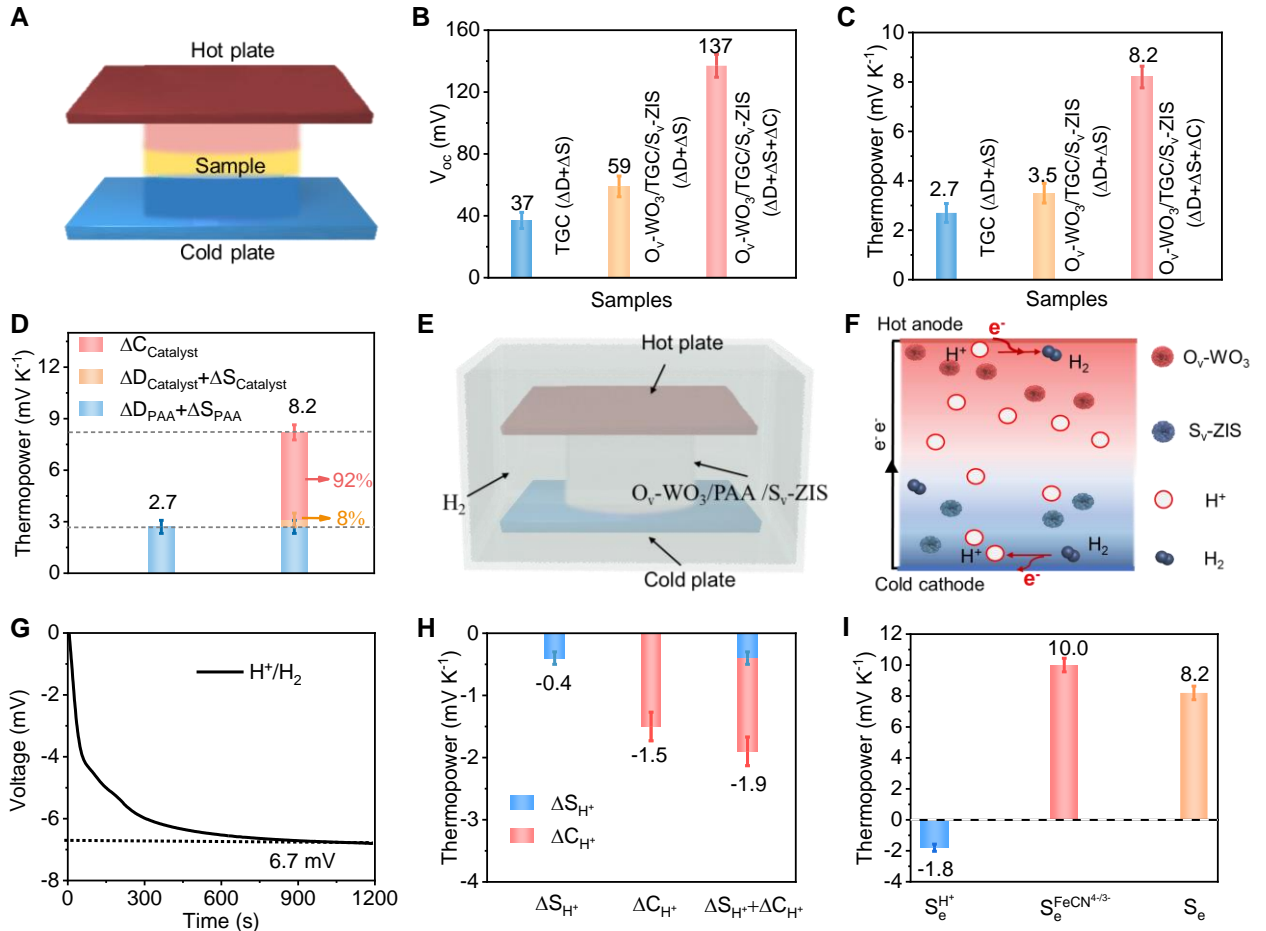


Fig. S12. The weight coefficient of ΔD , ΔS , and ΔC in the $O_v\text{-WO}_3/\text{TGC}/S_v\text{-ZIS}$ system. (A) Schematic of measurement setup for $O_v\text{-WO}_3/\text{TGC}/S_v\text{-ZIS}$ driven by $\Delta D + \Delta S$ with the temperature gradient. The ΔT in the system

was controlled by an electrical heating plate (on the top) and a water-cooled plate (on the bottom). **(B)** V_{oc} and **(C)** thermopower of TGC ($\Delta D + \Delta S$), $O_v\text{-}WO_3/\text{TGC}/S_v\text{-}ZIS$ ($\Delta D + \Delta S$), and $O_v\text{-}WO_3/\text{TGC}/S_v\text{-}ZIS$ ($\Delta D + \Delta S + \Delta C$). Error bars denoted the standard deviation from ten times repeated measurements. **(D)** Relative contributions of ΔS and ΔC with photocatalysts to the enhanced thermopower. **(E)** Reaction equipment and **(F)** schematic depiction of the thermogalvanic reaction of H^+/H_2 in the $O_v\text{-}WO_3/\text{PAA}/S_v\text{-}ZIS$ system. **(G)** Open-circuit voltage response versus time curve of $O_v\text{-}WO_3/\text{PAA}/S_v\text{-}ZIS$ for H^+/H_2 under light irradiation. **(H)** The contribution thermopower of H^+ concentration gradient in the system. **(I)** Relative contributions of H^+ and $FeCN^{4-/3-}$ in the $O_v\text{-}WO_3/\text{TGC}/S_v\text{-}ZIS$ system to the thermopower.

H^+ contribution: Two methods can be used to calculate the contribution of proton (H^+) gradient to thermopower.

Method one: The total thermopower of proton gradient ($S_e^{H^+}$) was the combination of the thermopower of H^+/H_2 ($S_{\Delta S}^{H^+}$) driven by the ΔS and the concentration gradient of proton between the hot and cold sides of system ($S_{\Delta C}^{H^+}$) based on Nernst equation of Eq. 8:

$$S_e^{H^+} = S_{\Delta S}^{H^+} + S_{\Delta C}^{H^+} \quad (8)$$

The thermopower of H^+/H_2 ($S_{\Delta S}^{H^+}$) driven by the ΔS in the $O_v\text{-}WO_3/\text{TGC}/S_v\text{-}ZIS$ system under light irradiation was not directly acquired due to the presence of the $FeCN^{4-/3-}$ in the system. To address this, we designed an $O_v\text{-}WO_3/\text{PAA}/S_v\text{-}ZIS$ system (without $FeCN^{4-/3-}$) to simulate the contribution of the entropy difference of H^+/H_2 thermogalvanic reaction produced by the $O_v\text{-}WO_3/\text{TGC}/S_v\text{-}ZIS$ system during photocatalytic reaction to the thermopower (**Figs. S12E and F**). Because the temperature difference was 16.8 K, a pH value of the hot side was 6.4, and the hydrogen production was $11 \mu\text{mol mL}^{-1}$ in the $O_v\text{-}WO_3/\text{TGC}/S_v\text{-}ZIS$ system under light irradiation, we simulated the temperature difference between the hot and cold sides of the $O_v\text{-}WO_3/\text{PAA}$ without $FeCN^{4-/3-}/S_v\text{-}ZIS$ system using a heating and cooling plate to maintain it at 16.8 K, controlled the pH value of the system as 6.4, and introduced $11 \mu\text{mol mL}^{-1}$ of hydrogen gas into the reactor. Based on the open-circuit voltage response versus time curve of $O_v\text{-}WO_3/\text{PAA}$ without $FeCN^{4-/3-}/S_v\text{-}ZIS$ for H^+/H_2 under light irradiation, the voltage (ΔV) of the system measured was -6.7 mV (**Fig. S12G**); and $S_{\Delta S}^{H^+}$ was -0.4 mV K^{-1} (i.e., $\frac{\Delta V}{\Delta T} = \frac{-6.7}{16.8} = -0.4$) (**Fig. S12H**). $S_{\Delta S}^{H^+}$ had a negative impact on the enhancement of thermopower in the $O_v\text{-}WO_3/\text{TGC}/S_v\text{-}ZIS$ system.

The contribution of the proton concentration gradient to the thermopower ($S_{\Delta C}^{H^+}$) was calculated according to Eq. 9:

$$\begin{aligned} S_{\Delta C}^{H^+} &= -\frac{R}{nF\Delta T} \left[T_{\text{hot}} \ln C_{\text{hot}}^{H^+} - T_{\text{cold}} \ln C_{\text{cold}}^{H^+} \right] \\ &= -\frac{8.314}{96485 \times 16.8} \times (315.4 \times \ln 3.9 \times 10^{-7} - 298.6 \times \ln 0.6 \times 10^{-7}) = -1.5 \end{aligned} \quad (9)$$

where $C_{\text{hot}}^{\text{H}^+}$ and $C_{\text{cold}}^{\text{H}^+}$ are the H^+ concentrations of hot and cold side, respectively. F , n , and R are the Faraday constant, the number of electrons transferred during a redox reaction, and the ideal gas constant, respectively. T_{hot} and T_{cold} are the temperatures of the hot and cold electrodes, respectively. H^+ concentrations can be obtained based on pH values of 6.4 (H^+ concentration: $3.9 \times 10^{-7} \text{ mol L}^{-1}$) and 7.2 (H^+ concentration: $0.6 \times 10^{-7} \text{ mol L}^{-1}$) on the hot and cold sides of the system, respectively. The thermopower ($S_{\Delta C}^{\text{H}^+}$) was calculated to be -1.5 mV K^{-1} . Finally, the proton gradient generated in our system contributed a total of -1.9 mV K^{-1} to thermopower (i.e., $-0.4 - 1.5 = -1.9$). It was noted that the concentration gradient of H^+ had an inverse effect on the increase in thermopower of $\text{FeCN}^{4-/3-}$ in the system.

Method two: The contribution of the proton gradient to the thermopower of the system can also be calculated based on the Eq. 10:

$$S_e = S_{\Delta D} + S_{\Delta S}^{\text{FeCN}^{4-/3-}} + S_{\Delta C}^{\text{FeCN}^{4-/3-}} + S_{\Delta S}^{\text{H}^+} + S_{\Delta C}^{\text{H}^+} \quad (10)$$

where S_e is the total thermopower in the $\text{O}_v\text{-WO}_3/\text{TGC}/\text{S}_v\text{-ZIS}$ system. $S_{\Delta D}$ is the thermodiffusion thermopower of mobile ions (i.e., K^+ , $\text{FeCN}^{4-/3-}$, H^+), and $S_{\Delta S}^{\text{FeCN}^{4-/3-}}$ is the thermopower driven by only solvent-dependent entropy difference (ΔS) of FeCN^{4-} and FeCN^{3-} . $S_{\Delta C}^{\text{FeCN}^{4-/3-}}$ is the thermopower driven by concentration difference (ΔC) of FeCN^{4-} and FeCN^{3-} . $S_{\Delta S}^{\text{H}^+}$ is thermopower driven by ΔS between H^+ and H_2 . $S_{\Delta C}^{\text{H}^+}$ is thermopower driven by ΔC of H^+ between hot and cold sides. In our system, we measured the value of S_e to be 8.2 mV K^{-1} . The measured value of $S_{\Delta D} + S_{\Delta S}^{\text{FeCN}^{4-/3-}}$ was 3.5 mV K^{-1} via the voltage measured for the system with the temperature difference of 16.8 K by designing the planar device (**Fig. S12B**). We calculated the theoretical $S_{\Delta C}^{\text{FeCN}^{4-/3-}}$ based on the concentrations of FeCN^{4-} and FeCN^{3-} on the hot and cold sides of the $\text{O}_v\text{-WO}_3/\text{TGC}/\text{S}_v\text{-ZIS}$ system by the Nernst equation. As detailed in Eq. 11:

$$\begin{aligned} S_{\Delta C}^{\text{FeCN}^{4-/3-}} &= \frac{R}{nF\Delta T} \left[T_{\text{hot}} \ln \frac{C_{\text{hot}}^{\text{FeCN}^{4-}}}{C_{\text{hot}}^{\text{FeCN}^{3-}}} - T_{\text{cold}} \ln \frac{C_{\text{cold}}^{\text{FeCN}^{4-}}}{C_{\text{cold}}^{\text{FeCN}^{3-}}} \right] \\ &= \frac{8.314}{96485 \times 16.8} \left[315.4 \ln \frac{0.56}{0.04} - 298.6 \ln \frac{0.12}{0.48} \right] = 6.5 \end{aligned} \quad (11)$$

where the $C_{\text{hot}}^{\text{FeCN}^{4-}}$ and $C_{\text{hot}}^{\text{FeCN}^{3-}}$ are measured to be 0.56 and 0.04 mol L^{-1} , respectively. The $C_{\text{cold}}^{\text{FeCN}^{4-}}$ and $C_{\text{cold}}^{\text{FeCN}^{3-}}$ are measured to be 0.12 and 0.48 mol L^{-1} , respectively. ΔT is 16.8 K . R is $8.314 \text{ J mol}^{-1} \text{ K}^{-1}$, F is 96485 C mol^{-1} , and the temperatures of the hot and cold sides are 315.4 and 298.6 K . The theoretical $S_{\Delta C}^{\text{FeCN}^{4-/3-}}$ of the $\text{O}_v\text{-WO}_3/\text{TGC}/\text{S}_v\text{-ZIS}$ system was calculated to be 6.5 mV K^{-1} . According to Eq. 11, the total thermopower of proton gradient ($S_{\Delta S}^{\text{H}^+} + S_{\Delta C}^{\text{H}^+}$) was calculated to be -1.8 mV K^{-1} ($8.2 - 3.5 - 6.5 = -1.8$) (**Table S1**). To sum up, the contribution of proton gradient to thermopower calculated from the two methods were similar, thus confirming the reliability of the experimental result.

Weight coefficient of $\text{FeCN}^{4-} + \text{FeCN}^{3-}$ contribution and H^+ contribution: We further investigated the specific contribution of the H^+ and $\text{FeCN}^{4-} + \text{FeCN}^{3-}$ to the total thermopower of system. The thermopower generated by the H^+ was -1.8 mV K^{-1} (**Fig. S12I**). Conversely, the thermopower of FeCN^{4-} and FeCN^{3-} contributed 10.0 mV K^{-1} (calculated from $3.5 + 6.5 = 10.0$). This result indicated that FeCN^{3-} and FeCN^{4-} played a crucial role in enhancing the thermopower of the system.

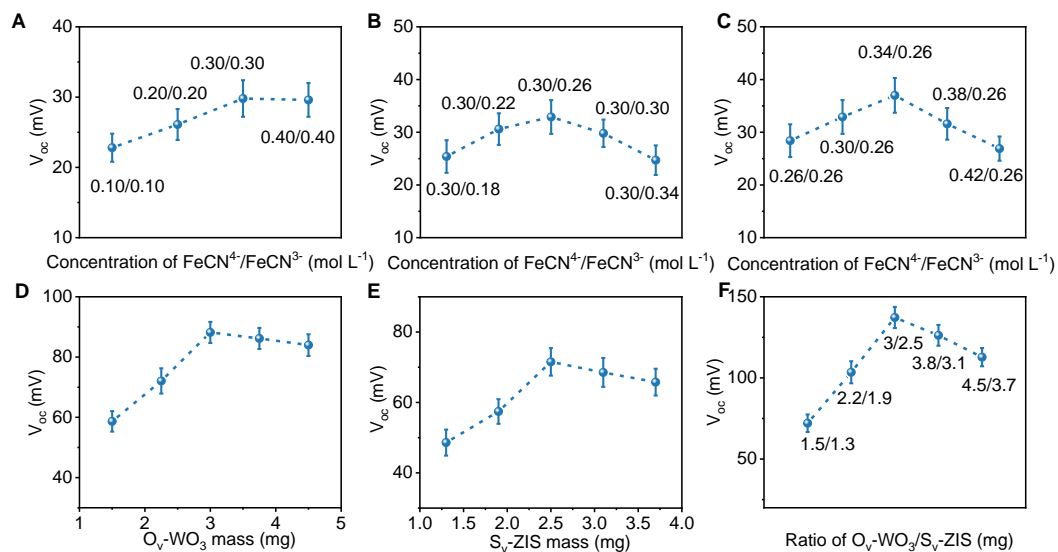


Fig. S13. The optimized amounts of $FeCN^{3-}$, $FeCN^4$, O_v-WO_3 , and S_v-ZIS in the system. (A) V_{oc} of TGC with varying concentrations of $FeCN^4$ and $FeCN^{3-}$ ($FeCN^4/FeCN^{3-}=0.10/0.10$, $0.20/0.20$, $0.30/0.30$, and $0.40/0.40$). (B) V_{oc} of TGC with $FeCN^4$ and varying concentrations of $FeCN^{3-}$ ($FeCN^4/FeCN^{3-}=0.30/0.18$, $0.30/0.22$, $0.30/0.26$, $0.30/0.30$, and $0.30/0.34$). (C) V_{oc} of TGC with $FeCN^{3-}$ and varying concentrations of $FeCN^4$ ($FeCN^4/FeCN^{3-}=0.26/0.26$, $0.30/0.26$, $0.34/0.26$, $0.38/0.26$, and $0.42/0.26$). (D) V_{oc} of O_v-WO_3 /TGC with varying contents of O_v-WO_3 . (E) V_{oc} of TGC/ S_v-ZIS with different contents of S_v-ZIS . (F) V_{oc} of O_v-WO_3 /TGC/ S_v-ZIS with differing contents of O_v-WO_3 and S_v-ZIS . Error bars denoted the standard deviation from ten times repeated measurements.

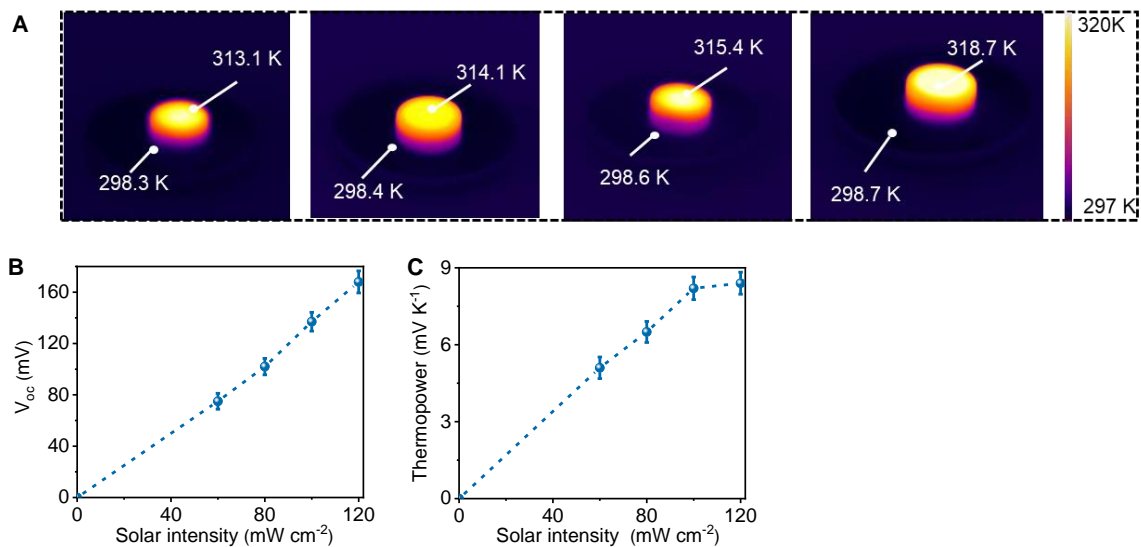


Fig. S14. The effect of light intensity on the thermopower of the system. (A) Infrared images of O_v-WO₃/TGC/S_v-ZIS with the electrodes under light irradiation with 60, 80, 100, and 120 mW cm⁻² solar intensity. (B) V_{oc} versus solar intensity (i.e., 60, 80, 100, and 120 mW cm⁻²) for O_v-WO₃/TGC/S_v-ZIS. (C) The thermopower versus solar intensity (i.e., 60, 80, 100, and 120 mW cm⁻²) for O_v-WO₃/TGC/S_v-ZIS. Error bars denoted the standard deviation from three times repeated measurements. The thermopower of our system increased with an increment in light intensity (results were 5.1, 6.5, 8.2, and 8.4 mV K⁻¹ for 60, 80, 100, and 120 mW cm⁻², respectively). These results indicated a positive correlation between thermopower and light intensity, which can be attributed to the photoredox ability of the photocatalysts under different solar light intensities.

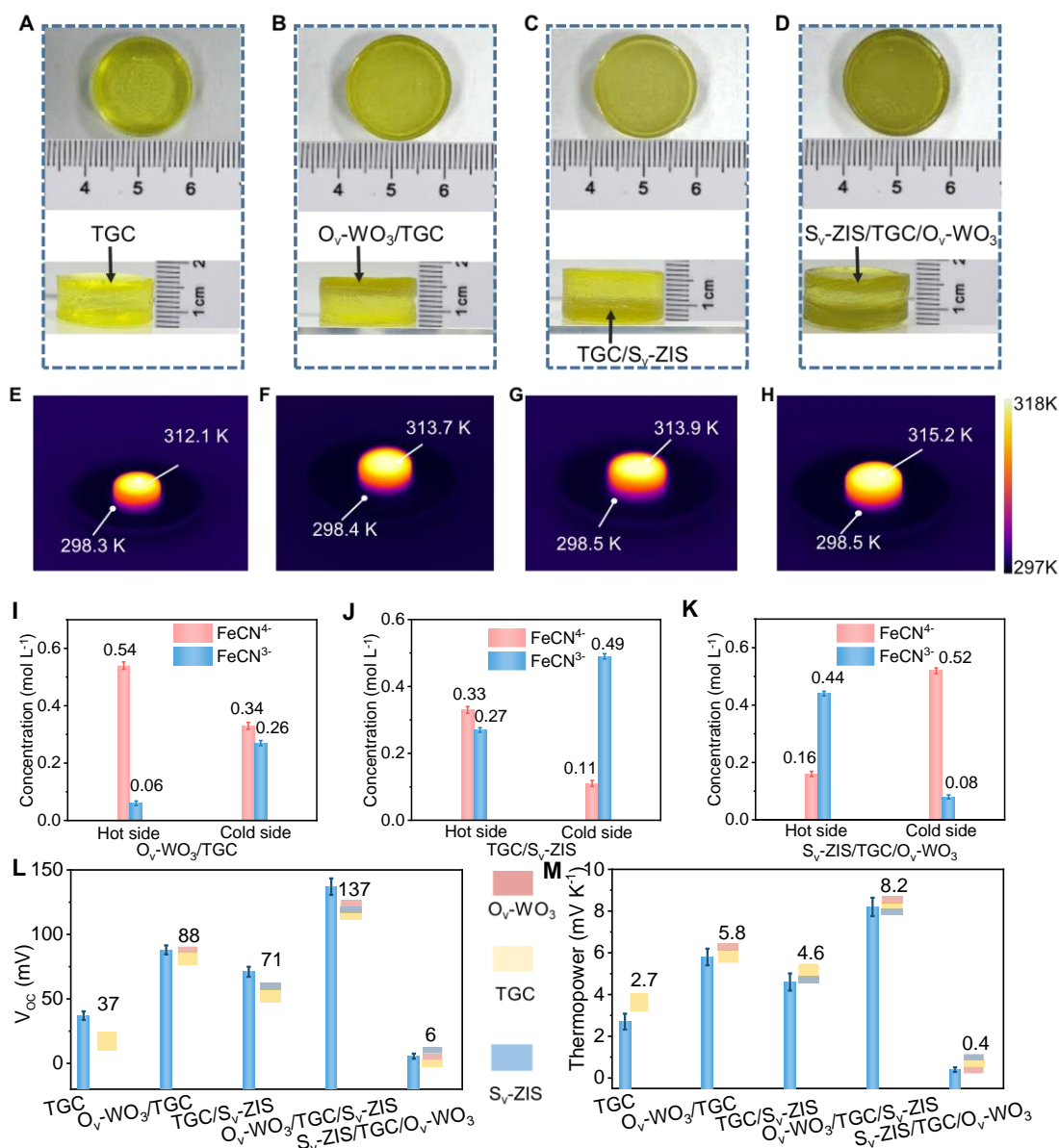


Fig. S15. The effect of locations for $O_v\text{-WO}_3$ and $S_v\text{-ZIS}$ on the thermopower of the system. Digital photographs of (A) TGC, (B) $O_v\text{-WO}_3/\text{TGC}$, (C) $\text{TGC}/S_v\text{-ZIS}$, and (D) $S_v\text{-ZIS}/\text{TGC}/O_v\text{-WO}_3$. Infrared thermal images of (E) TGC, (F) $O_v\text{-WO}_3/\text{TGC}$, (G) $\text{TGC}/S_v\text{-ZIS}$, and (H) $S_v\text{-ZIS}/\text{TGC}/O_v\text{-WO}_3$ with the electrodes. Concentrations of FeCN^{4-} and FeCN^{3-} on the hot and cold sides of (I) $O_v\text{-WO}_3/\text{TGC}$, (J) $\text{TGC}/S_v\text{-ZIS}$, and (K) $S_v\text{-ZIS}/\text{TGC}/O_v\text{-WO}_3$ systems after 60 min light irradiation, respectively. (L) V_{oc} and (M) thermopowers of TGC, $O_v\text{-WO}_3/\text{TGC}$, $\text{TGC}/S_v\text{-ZIS}$, $O_v\text{-WO}_3/\text{TGC}/S_v\text{-ZIS}$, and $S_v\text{-ZIS}/\text{TGC}/O_v\text{-WO}_3$. Error bars denoted the standard deviation from three times repeated measurements. The locations of $O_v\text{-WO}_3$ and $S_v\text{-ZIS}$ were crucial to the thermoelectric performance. When only $O_v\text{-WO}_3$ was added to the hot side or only $S_v\text{-ZIS}$ was introduced to the cold side, the thermopower values increased to 5.8 mV K^{-1} or 4.6 mV K^{-1} , respectively, due to the limited enhancement of ΔC for FeCN^{4-} and FeCN^{3-} between two sides. Conversely, when $O_v\text{-WO}_3$ and $S_v\text{-ZIS}$ were added to cold and hot sides, respectively, the thermopower of $S_v\text{-ZIS}/\text{TGC}/O_v\text{-WO}_3$ was significantly reduced to 0.4 mV K^{-1} due to the opposing effects, i.e., ΔS and the catalyst-enhanced ΔC . These results further demonstrated that the photocatalytic process induced a continuous ΔC and thus significantly improved the thermopower of TGC.

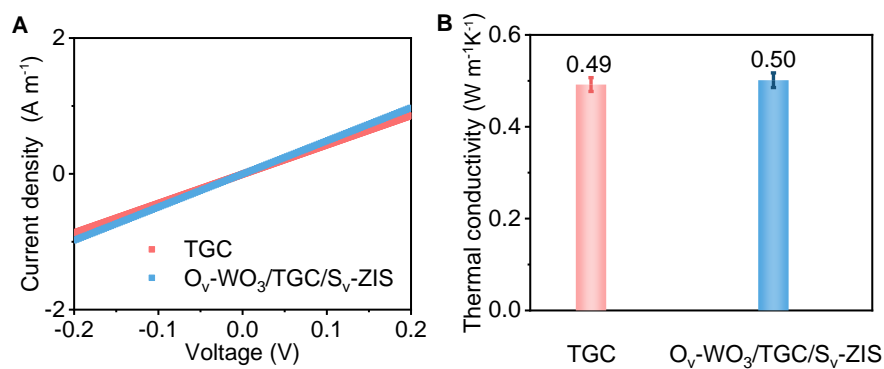


Fig. S16. The electrical conductivities and thermal conductivities. (A) Current-voltage (I-V) curves and (B) thermal conductivities of O_v-WO₃/TGC/S_v-ZIS and TGC. Error bars denoted the standard deviation from three times repeated measurements. The electrical conductivity of the sample was calculated from the slope of the I-V curve. The electrical conductivities of TGC and O_v-WO₃/TGC/S_v-ZIS were 4.2 and 4.7 S m⁻¹, respectively (**Fig. S16A**). Their thermal conductivities were 0.49 W m⁻¹ K⁻¹ for TGC and 0.50 W m⁻¹ K⁻¹ for O_v-WO₃/TGC/S_v-ZIS (**Fig. S16B**).

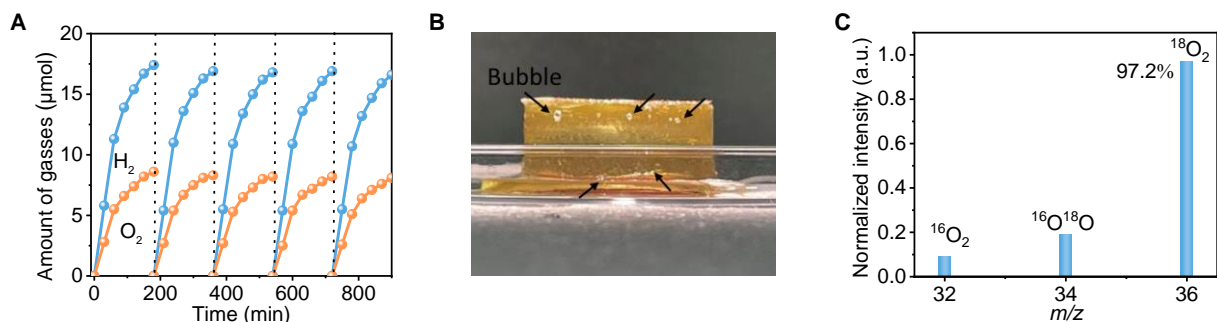


Fig. S17. The photocatalytic performances. (A) Repeated cycles of overall photocatalytic water splitting for O_v-WO₃/TGC/S_v-ZIS. (B) Digital photograph of gas release in the O_v-WO₃/TGC/S_v-ZIS system. The hydrogen and oxygen evolution rates using O_v-WO₃/TGC/S_v-ZIS were shown in **Fig. 2E** of the main text. (C) Mass spectrum of oxygen gas evolved during photocatalytic H₂O¹⁸ splitting over O_v-WO₃/TGC/S_v-ZIS system. In the process of preparing O_v-WO₃/TGC/S_v-ZIS, H₂¹⁸O replaced deionized water. Additionally, the deionized water in the reactor was also replaced by H₂¹⁸O.

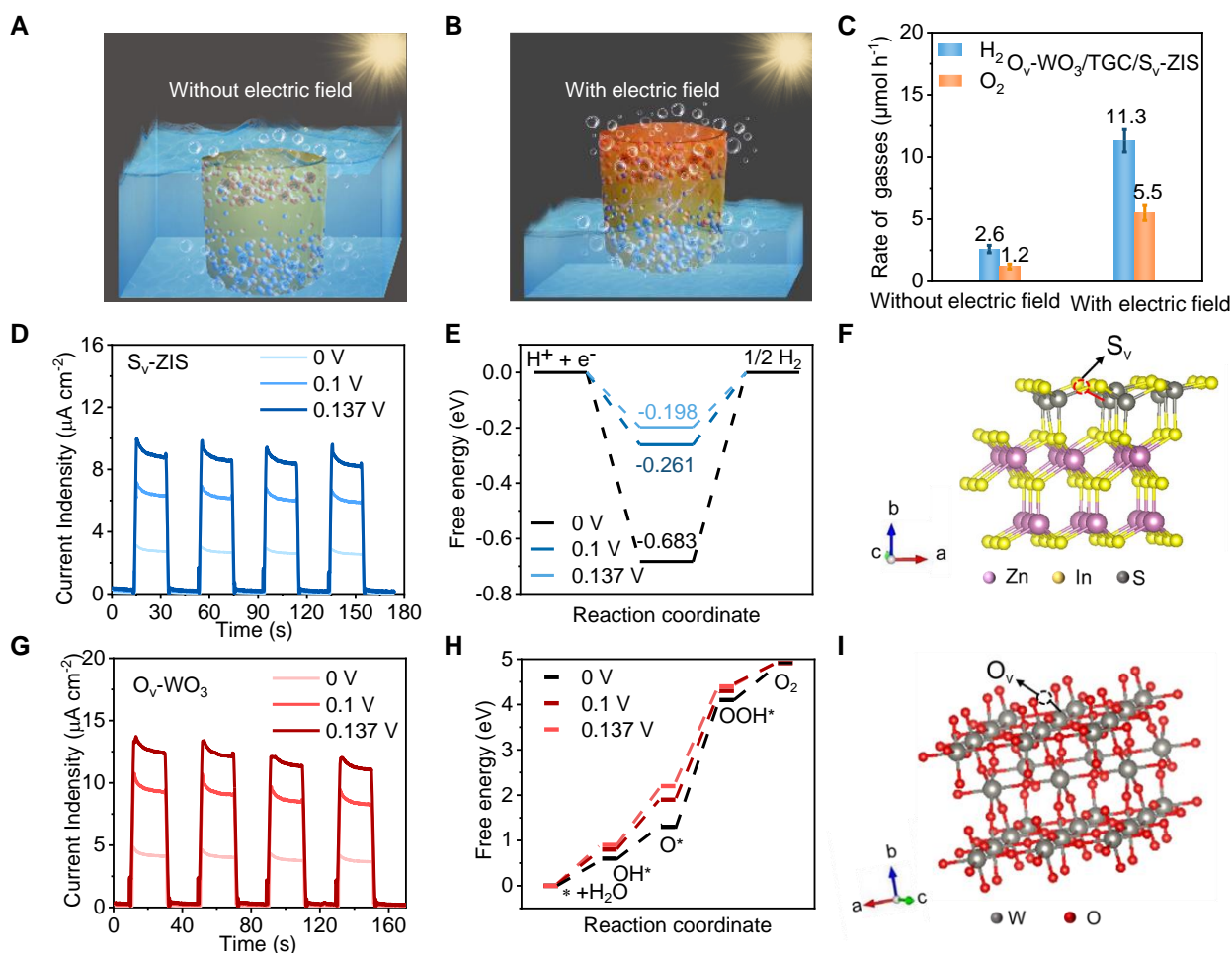


Fig. S18. Photocatalytic behavior of photocatalysts in the photocatalytically enhanced thermogalvanic system.

Schematic diagram of the photocatalytic reaction of $\text{O}_v\text{-WO}_3/\text{TGC}/\text{S}_v\text{-ZIS}$ (A) without and (B) with an electric field under light irradiation. (C) Hydrogen and oxygen evolution rates using $\text{O}_v\text{-WO}_3/\text{TGC}/\text{S}_v\text{-ZIS}$ with and without an electric field. Error bars denoted the standard deviation from ten times repeated measurements. (D) Transient photocurrent curves of $\text{S}_v\text{-ZIS}$ at different voltages (0, 0.1, and 0.137 V). (E) Free energy diagram for H_2 evolution of $\text{S}_v\text{-ZIS}$ at different voltages (0, 0.1, and 0.137 V). (F) Structural model of $\text{S}_v\text{-ZIS}$. (G) Transient photocurrent curves of $\text{O}_v\text{-WO}_3$ at different voltages (0, 0.1, and 0.137 V). (H) Free energy diagram for O_2 evolution of $\text{O}_v\text{-WO}_3$ at different voltages (0, 0.1, and 0.137 V). (I) Structural model of $\text{O}_v\text{-WO}_3$. We conducted the DFT calculations on electric field effect (0.137 V) condition to investigate the Gibbs free energy (ΔG) of the H_2 evolution and O_2 evolution processes. The ΔG of H_{ads} (H^* adsorption on $\text{S}_v\text{-ZIS}$) was -0.683 eV at 0 V and changed to -0.198 eV at 0.137 V (Fig. S18E). Free energy profiles of $\text{O}_v\text{-WO}_3$ during the O_2 evolution process were presented in Fig. S18H. The free energy change of the third elementary step was higher than that of other elementary steps, indicating that the formation of OOH^* from O^* was the rate-determining step (RDS) of $\text{O}_v\text{-WO}_3$. The free energy barrier of RDS was significantly reduced to 2.2 eV from 2.8 eV when an electric field (0.137 V) was introduced, confirming that an external field was thermodynamically favorable for both H_2 and O_2 evolution of photocatalysts.

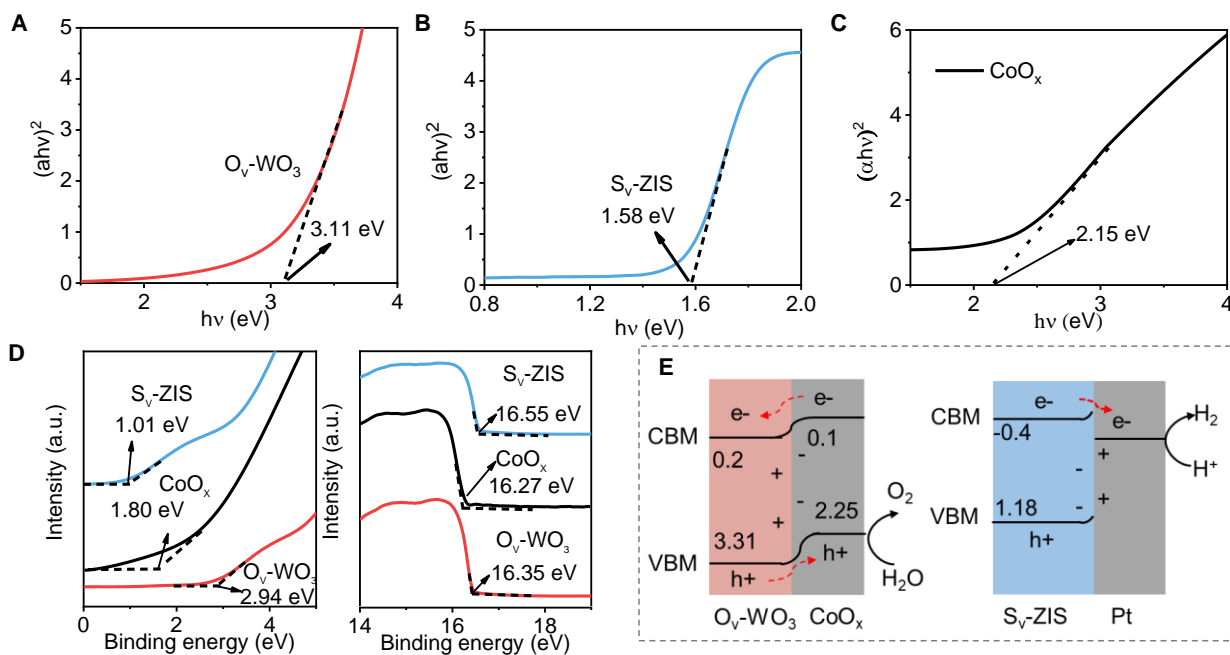


Fig. S19. The band structures. Diagrams of band gap for (A) $O_v\text{-WO}_3$, (B) $S_v\text{-ZIS}$, and (C) CoO_x . (D) VB XPS spectra and UPS spectra of $O_v\text{-WO}_3$, $S_v\text{-ZIS}$, and CoO_x . (E) Band structure of $\text{CoO}_x/O_v\text{-WO}_3$ and $\text{Pt}/S_v\text{-ZIS}$. Based on the Kubelka–Munk function, the band gap diagram was obtained by UV-vis DRS spectra (20). The optical band gaps of $O_v\text{-WO}_3$, $S_v\text{-ZIS}$, and CoO_x were 3.11, 1.58, and 2.15 eV, respectively. As displayed in **Figs. S19A–D**, the valence band maximum (VBM) potential (E_{VBM}) of $O_v\text{-WO}_3$, $S_v\text{-ZIS}$, and CoO_x were calculated to be -7.81, -5.68, and -6.75 eV (vs. Vacuum), respectively (25). Hence, the E_{VBM} of $O_v\text{-WO}_3$, $S_v\text{-ZIS}$, and CoO_x can be determined as 3.31, 1.18, 2.25 eV (vs. NHE), respectively. Furthermore, by combining the bandgaps of samples, the conduction band minimum (CBM) potential (E_{CBM}) of $O_v\text{-WO}_3$, $S_v\text{-ZIS}$, and CoO_x could be obtained to be 0.2, -0.4, and 0.1 eV, respectively.

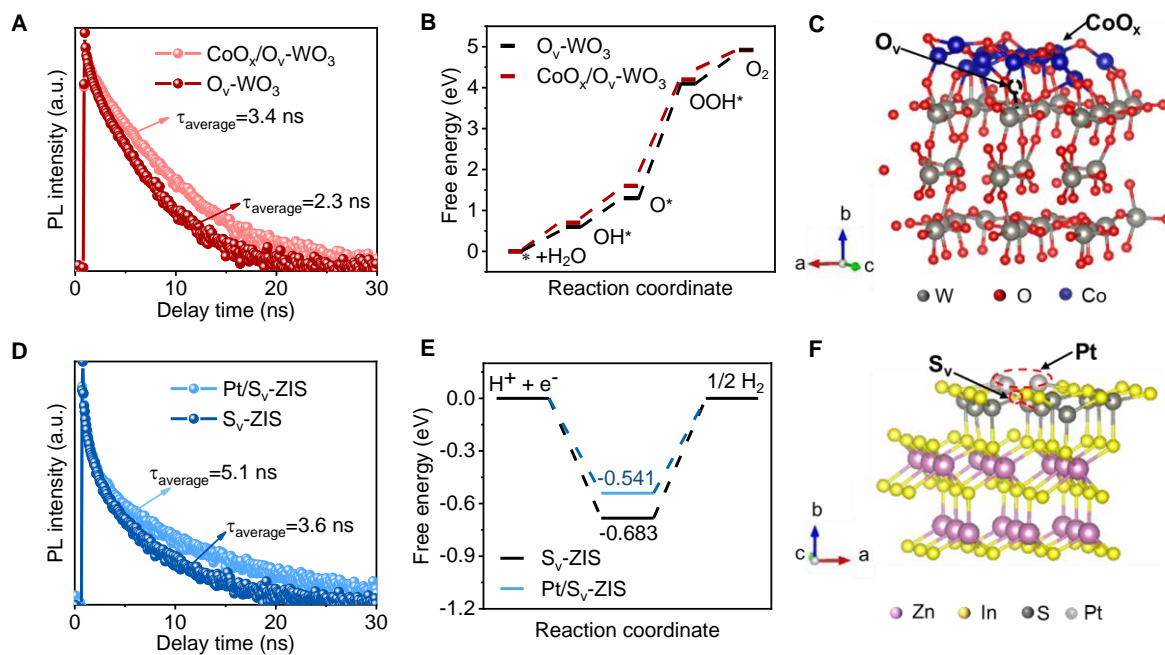


Fig. S20. The roles of CoO_x and Pt. (A) Time-resolved PL spectra of O_v-WO₃ and CoO_x/O_v-WO₃. (B) Free energy diagram for O₂ evolution of O_v-WO₃ and CoO_x/O_v-WO₃. (C) Structural model of CoO_x/O_v-WO₃. (D) Time-resolved PL spectra of S_v-ZIS and Pt/S_v-ZIS. (E) Free energy diagram for H₂ evolution of S_v-ZIS and Pt/S_v-ZIS. (F) Structural model of Pt/S_v-ZIS. The CoO_x and Pt co-catalysts played important roles in extracting photogenerated carriers and providing active sites to accelerate the photocatalytic H₂ and O₂ evolution.

Note S2. The H^+ generation and migration in the $O_v\text{-WO}_3/\text{TGC}/S_v\text{-ZIS}$ system

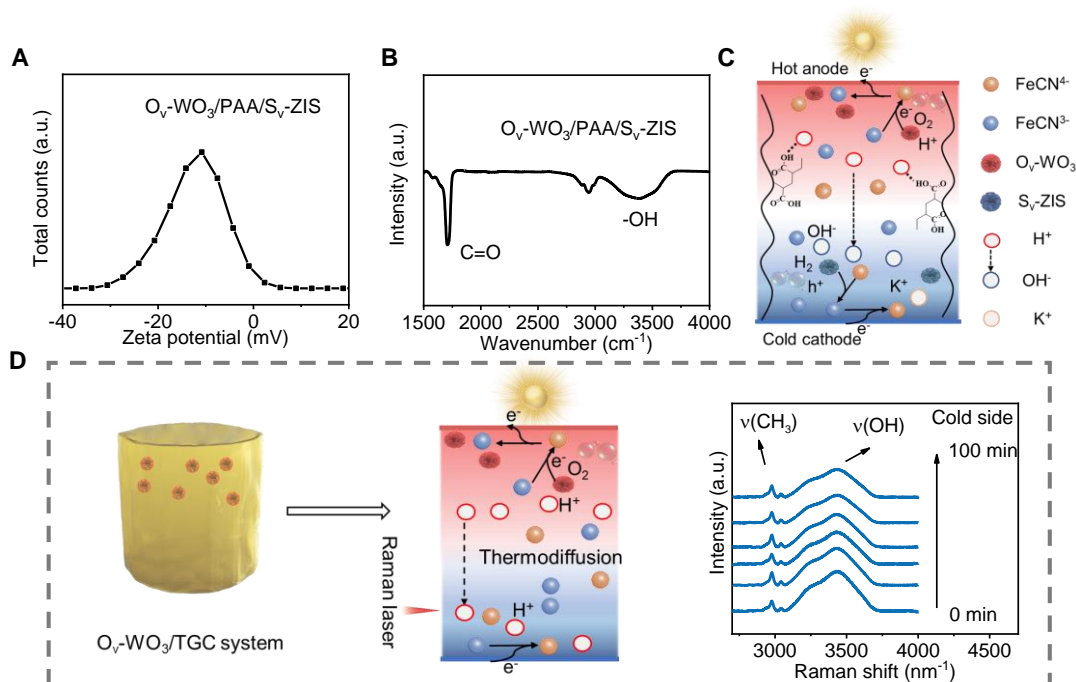


Fig. S21. H^+ generation and transport. (A) Zeta potential measurement of $O_v\text{-WO}_3/\text{PAA}/S_v\text{-ZIS}$. (B) FTIR spectrum of $O_v\text{-WO}_3/\text{PAA}/S_v\text{-ZIS}$. (C) Working principle of protonation and thermoeffusion for the H^+ in the $O_v\text{-WO}_3/\text{TGC}/S_v\text{-ZIS}$ under the light illumination. (D) Real-time of water structure monitoring of $O_v\text{-WO}_3/\text{TGC}$ through in situ Raman study.

To explore the reasons for forming a small H^+ gradient, we considered two aspects: the protonation and deprotonation processes in the matrix and the thermoeffusion of H^+ . From the perspective of protonation, the Zeta potential measurement confirmed the negatively charged surface of PAA (**Fig. S21 A**), which was mainly attributed to the carboxyl groups $-\text{COOH}$ stretch in the PAA matrix, as shown in FTIR spectroscopy (**Fig. S21 B**). According to Manning's "counterion condensation" theory, some H^+ cations produced on the hot side tended to adhere along negatively charged polymer chains under temperature gradient in our system (**Fig. S21 C**). From the perspective of thermoeffusion of H^+ , some H^+ cations that were not protonated to the negative polymer backbones thermoeffused to neutralize OH^- on the cold side. Boltzmann distribution theory revealed that the negatively charged surface subsequently attracted electrolyte cations to form electrical double layers, while repelling anions to realize a selective cations migration. The H^+ had higher thermophoretic mobility than OH^- and possessed a faster migration rate in the electrolyte because of their smaller radius. As proof, we designed the $O_v\text{-WO}_3/\text{TGC}$ system without $S_v\text{-ZIS}$ loading on the cold side, where only H^+ were produced on the hot side. We monitored the migration of H^+ via in situ Raman on the cold side of the $O_v\text{-WO}_3/\text{TGC}$ to confirm the thermoeffusion of H^+ cations. The O-H stretching peak intensities gradually decreased on the cold side of the system for up to 60 min (**Fig. S21 D**). This was because of H^+ forming on the hot side migrated to the cold side by thermoeffusion. Therefore, under the synergistic coupling of two factors, the H^+ gradient generated in our system was small (**Fig. S21 C**).

Note S3. Theoretical analysis of the relationship between the thermopower and H₂ production rate

For the thermogalvanic cell, based on the Nernst equation, the equilibrium potential ($A_{\text{ox}} + e^- \leftrightarrow B_{\text{red}}$) of the redox reaction can be described as (14):

$$E = E^0 + \frac{RT}{nF} \ln \frac{(a_{\text{ox}})^A}{(a_{\text{red}})^B} \quad (12)$$

where E is potential, E^0 is the standard potential, A and B are oxidized and reductive ions, respectively, a_{ox} and a_{red} are the activities of species A and B, respectively. R , T , n , and F are the ideal gas constant, temperature, the number of electrons transferred in the electrochemical reaction, and Faraday constant, respectively. The activity (α) is mentioned as the product of the activity coefficient (γ) and the concentration (C) (16).

$$E = E^0 + \frac{RT}{nF} \left[\ln \frac{(\gamma_{\text{ox}})^A}{(\gamma_{\text{red}})^B} + \ln \frac{(C_{\text{ox}})^A}{(C_{\text{red}})^B} \right] \quad (13)$$

where γ_{ox} and γ_{red} are activity coefficients of species A and B, respectively, C_{ox} and C_{red} are species A and B concentrations, respectively.

Based on Eq. 1 $S = -\frac{E_{\text{hot}} - E_{\text{cold}}}{T_{\text{hot}} - T_{\text{cold}}}$, where S is the thermogalvanic thermopower, the subscripts “hot” and “cold” indicate the corresponding variables pertaining to the hot and cold sides (6, 21). e.g., T_{hot} and T_{cold} are the temperatures at the hot and cold sides of the sample, respectively.

Therefore, S can be finally written as the sum of two terms.

$$S = -\frac{R}{nF\Delta T} \left[T_{\text{hot}} \ln \frac{(\gamma_{\text{ox}})_{\text{hot}}^A}{(\gamma_{\text{red}})_{\text{hot}}^B} - T_{\text{cold}} \ln \frac{(\gamma_{\text{ox}})_{\text{cold}}^A}{(\gamma_{\text{red}})_{\text{cold}}^B} \right] - \frac{R}{nF\Delta T} \left[T_{\text{hot}} \ln \frac{(C_{\text{ox}})_{\text{hot}}^A}{(C_{\text{red}})_{\text{hot}}^B} - T_{\text{cold}} \ln \frac{(C_{\text{ox}})_{\text{cold}}^A}{(C_{\text{red}})_{\text{cold}}^B} \right] \quad (14)$$

The first term is only related to the activity coefficient (γ), which is dominated by the solvent-dependent difference in entropy (ΔS) between the redox ions (1). The second term is only related to the concentrations difference (ΔC) of A and B. We can calculate the thermopower based on Eq. 14 for all thermogalvanic cells.

The thermopower of the system arises from the combined influence of thermodiffusion and thermogalvanic effects. The thermodiffusion thermopower $S_{\Delta D}$ can be defined as:

$$S_{\Delta D} = \frac{\partial E}{\partial T} \approx \frac{\sum(\mu_{E,+}) - \sum(\mu_{E,-})}{\sum(\mu_{N,+}) - \sum(\mu_{N,-})} \quad (15)$$

where $\mu_{E,+/-}$ and $\mu_{N,+/-}$ are thermal and electrical mobility of cations (K^+ and H^+) and anions ($FeCN^{3-}$ and $FeCN^{4-}$).

Contribution of FeCN^{3-} and FeCN^{4-} to the thermopower

Regarding our $\text{O}_v\text{-WO}_3/\text{TGC}/\text{S}_v\text{-ZIS}$ system, the redox couple is FeCN^{3-} and FeCN^{4-} . The FeCN^{4-} and FeCN^{3-} concentrations vary during the photocatalytic reaction. In addition, the thermopower of our system is influenced by the thermodiffusion of K^+ , H^+ , FeCN^{3-} , and FeCN^{4-} . Hence, the thermopower of such a system can be calculated by:

$$S_e^{\text{FeCN}^{4-/3-}} = \frac{\sum(\mu_{E,+}) - \sum(\mu_{E,-})}{\sum(\mu_{N,+}) - \sum(\mu_{N,-})} + \frac{R}{nF\Delta T} \left[T_{\text{hot}} \ln \frac{(\gamma^{\text{FeCN}^{4-}})_{\text{hot}}}{(\gamma^{\text{FeCN}^{3-}})_{\text{hot}}} - T_{\text{cold}} \ln \frac{(\gamma^{\text{FeCN}^{4-}})_{\text{cold}}}{(\gamma^{\text{FeCN}^{3-}})_{\text{cold}}} \right] + \frac{R}{nF\Delta T} \left[T_{\text{hot}} \ln \frac{(C_0^{\text{FeCN}^{4-}} + C_x)_{\text{hot}}}{(C_0^{\text{FeCN}^{3-}} - C_x)_{\text{hot}}} - T_{\text{cold}} \ln \frac{(C_0^{\text{FeCN}^{4-}} - C_x)_{\text{cold}}}{(C_0^{\text{FeCN}^{3-}} + C_x)_{\text{cold}}} \right] \quad (16)$$

where $\gamma^{\text{FeCN}^{4-}}$ and $\gamma^{\text{FeCN}^{3-}}$ are the activity coefficients of FeCN^{4-} and FeCN^{3-} , respectively. $C_0^{\text{FeCN}^{4-}}$ and $C_0^{\text{FeCN}^{3-}}$ are original concentrations of FeCN^{4-} and FeCN^{3-} , respectively. C_x is the concentration variation during the photocatalytic reaction. Since the first term can be simplified as the constant $S_{\Delta D}$ driven by thermodiffusion of mobile ions (i.e., K^+ , $\text{FeCN}^{4-/3-}$, H^+) and the second term can be simplified as the constant $S_{\Delta S}$ driven by ΔS , the Eq. 16 can also be expressed as:

$$S_e^{\text{FeCN}^{4-/3-}} = S_{\Delta D} + S_{\Delta S}^{\text{FeCN}^{4-/3-}} + \frac{R}{nF\Delta T} \left[T_{\text{hot}} \ln \frac{(C_0^{\text{FeCN}^{4-}} + C_x)_{\text{hot}}}{(C_0^{\text{FeCN}^{3-}} - C_x)_{\text{hot}}} - T_{\text{cold}} \ln \frac{(C_0^{\text{FeCN}^{4-}} - C_x)_{\text{cold}}}{(C_0^{\text{FeCN}^{3-}} + C_x)_{\text{cold}}} \right] \quad (17)$$

Contribution of H^+ to the thermopower

In addition, a small H^+ gradient formed in the $\text{O}_v\text{-WO}_3/\text{TGC}/\text{S}_v\text{-ZIS}$ system, which contributed to the thermopower.

$$S_e^{\text{H}^+} = S_{\Delta S}^{\text{H}^+} + S_{\Delta C}^{\text{H}^+} = S_{\Delta S}^{\text{H}^+} + \frac{R}{nF\Delta T} \left[T_{\text{hot}} \ln C_{\text{hot}}^{\text{H}^+} - T_{\text{cold}} \ln C_{\text{cold}}^{\text{H}^+} \right] \quad (18)$$

where $S_{\Delta S}^{\text{H}^+}$ is the thermopower driven by ΔS of H^+/H_2 . $S_{\Delta C}^{\text{H}^+}$ is the thermopower driven by ΔC of H^+ . $C_{\text{hot}}^{\text{H}^+}$ and $C_{\text{cold}}^{\text{H}^+}$ are the H^+ concentrations of hot and cold side, respectively. Thus, the total thermopower of $\text{O}_v\text{-WO}_3/\text{TGC}/\text{S}_v\text{-ZIS}$ system is the sum of $S_e^{\text{FeCN}^{4-/3-}}$ and $S_e^{\text{H}^+}$.

$$S_e = S_e^{\text{FeCN}^{4-/3-}} + S_e^{\text{H}^+} \quad (19)$$

$$S_e = S_{\Delta D} + S_{\Delta S}^{\text{FeCN}^{4-/3-}} + \frac{R}{nF\Delta T} \left[T_{\text{hot}} \ln \frac{(C_0^{\text{FeCN}^{4-}} + C_x)_{\text{hot}}}{(C_0^{\text{FeCN}^{3-}} - C_x)_{\text{hot}}} - T_{\text{cold}} \ln \frac{(C_0^{\text{FeCN}^{4-}} - C_x)_{\text{cold}}}{(C_0^{\text{FeCN}^{3-}} + C_x)_{\text{cold}}} \right] + S_e^{\text{H}^+} \quad (20)$$

According to the working principle of the photocatalytically enhanced thermogalvanic system and the Nernst equation between the thermopower and redox concentration, the electrons exchange between the redox reaction ($\text{FeCN}^{3-} + e^- \leftrightarrow \text{FeCN}^{4-}$) at the hot and cold sides accompany by the photocatalytic water splitting (i.e., one H_2 molecule production along with two FeCN^{4-} oxide to FeCN^{3-} on the cold side, while one O_2 molecular production converts four FeCN^{3-} to FeCN^{4-} on the hot side). In this study, we focused on the relatively steady-state system that was achieved after 1 hour of light

irradiation, during which the amount of H₂ produced equaled the H₂ production rate. The FeCN⁴⁻ or FeCN³⁻ concentration variation C_x is equal to $\frac{2x}{V_c}$ (x and V_c are the H₂ production rate and the volume of the electrolyte solution of the hydrogen-evolution photocatalyst, respectively). Assuming an ideal scenario where the stoichiometric ratio of hydrogen and oxygen production in the photocatalytic water splitting process is 2:1, and the generated electrons or holes are completely utilized in the redox reaction (FeCN³⁻+e⁻↔FeCN⁴⁻) in the system, we can derive the theoretical Eq. 21 between thermopower and H₂ production rate based on Eq. 20:

$$S_e = S_{\Delta D} + S_{\Delta S}^{\text{FeCN}^{4-/3-}} + \frac{R}{nF\Delta T} \left[T_{\text{hot}} \ln \frac{C_0^{\text{FeCN}^{4-}} + 2x/V_c}{C_0^{\text{FeCN}^{3-}} - 2x/V_c} - T_{\text{cold}} \ln \frac{C_0^{\text{FeCN}^{4-}} - 2x/V_c}{C_0^{\text{FeCN}^{3-}} + 2x/V_c} \right] + S_e^{\text{H}^+} \quad (21)$$

We extend this Eq. 21 to formal power series as follow:

$$S_e = S_{\Delta D} + S_{\Delta S}^{\text{FeCN}^{4-/3-}} + \frac{R}{nF\Delta T} \left\{ T_{\text{hot}} \left[\sum_{n=1}^{\infty} \frac{-1^{n-1} \left(\frac{2x}{C_0^{\text{FeCN}^{4-}} V_c} \right)^n}{n} - \sum_{n=1}^{\infty} \frac{-1^{n-1} \left(\frac{2x}{C_0^{\text{FeCN}^{3-}} V_c} \right)^n}{n} + \ln C_0^{\text{FeCN}^{4-}} - \ln C_0^{\text{FeCN}^{3-}} \right] - \right. \\ \left. T_{\text{cold}} \left[\sum_{n=1}^{\infty} \frac{-1^{n-1} \left(\frac{2x}{C_0^{\text{FeCN}^{4-}} V_c} \right)^n}{n} - \sum_{n=1}^{\infty} \frac{-1^{n-1} \left(\frac{2x}{C_0^{\text{FeCN}^{3-}} V_c} \right)^n}{n} + \ln C_0^{\text{FeCN}^{4-}} - \ln C_0^{\text{FeCN}^{3-}} \right] \right\} + S_e^{\text{H}^+} \quad (22)$$

The equation is expanded into the following expression:

$$S_e = S_{\Delta D} + S_{\Delta S}^{\text{FeCN}^{4-/3-}} + \frac{R}{nF} \left(\ln C_0^{\text{FeCN}^{4-}} - \ln C_0^{\text{FeCN}^{3-}} \right) + \frac{2R}{nF\Delta T} (T_{\text{hot}} + T_{\text{cold}}) \left(\frac{1}{C_0^{\text{FeCN}^{4-}} V_c} + \frac{1}{C_0^{\text{FeCN}^{3-}} V_c} \right) x + \\ \frac{2R}{nF} \left(\frac{1}{(C_0^{\text{FeCN}^{4-}} V_c)^2} - \frac{1}{(C_0^{\text{FeCN}^{3-}} V_c)^2} \right) x^2 + \frac{8R}{nF\Delta T} \frac{T_{\text{hot}} + T_{\text{cold}}}{3} \left(\frac{1}{(C_0^{\text{FeCN}^{4-}} V_c)^3} + \frac{1}{(C_0^{\text{FeCN}^{3-}} V_c)^3} \right) x^3 \dots \quad (23)$$

$$S_e = S_{\Delta D} + S_{\Delta S}^{\text{FeCN}^{4-/3-}} + \frac{R}{nF} \left(\ln C_0^{\text{FeCN}^{4-}} - \ln C_0^{\text{FeCN}^{3-}} \right) + \frac{2R}{nF\Delta T} (T_{\text{hot}} + T_{\text{cold}}) \left(\frac{1}{C_0^{\text{FeCN}^{4-}} V_c} + \frac{1}{C_0^{\text{FeCN}^{3-}} V_c} \right) x + O_{(x)} + S_e^{\text{H}^+} \quad (24)$$

where x is in the range of $0 \leq x < \frac{C_0^{\text{FeCN}^{3-}} V_c}{2}$ and $0 \leq x < \frac{C_0^{\text{FeCN}^{4-}} V_c}{2}$, the $C_0^{\text{FeCN}^{4-}}$ and $C_0^{\text{FeCN}^{3-}}$ generally vary in the ranges $0 < C_0^{\text{FeCN}^{4-}}, 0 < C_0^{\text{FeCN}^{3-}}, 0 < C_0^{\text{FeCN}^{4-}} + C_0^{\text{FeCN}^{3-}} < \text{saturated solubility of redox ions}$. As $\frac{1}{(C_0^{\text{FeCN}^{4-}} V_c)^2} - \frac{1}{(C_0^{\text{FeCN}^{3-}} V_c)^2} \rightarrow 0$ ($C_0^{\text{FeCN}^{4-}}$ and $C_0^{\text{FeCN}^{3-}}$ are close to ensuring the efficient redox reaction in

thermogalvanic cells (5)), the part of $n \geq 2$ is the infinitesimal of higher order and $O_{(x)}$ can be ignored to simplify the analysis. **Thus, the universal theoretical function relationship between thermopower and H₂ production rate was established for photocatalytically enhanced thermogalvanic cells, as shown in Eq. 25:**

$$S_e = S_{\Delta D} + S_{\Delta S}^{\text{FeCN}^{4-/3-}} + \frac{R}{nF} (\ln C_0^{\text{FeCN}^{4-}} - \ln C_0^{\text{FeCN}^{3-}}) + \frac{2R}{nF\Delta T} (T_{\text{hot}} + T_{\text{cold}}) \left(\frac{1}{C_0^{\text{FeCN}^{4-}} V_c} + \frac{1}{C_0^{\text{FeCN}^{3-}} V_c} \right) x + S_e^{\text{H}^+} \quad (25)$$

We further confirm the reliability of the simplified Eq. 25 in the system by substituting the corresponding parameter values. The FeCN^{3-} and FeCN^{4-} concentrations are 0.26 and 0.34 mol L⁻¹. ΔT is 16.8 K. The volume of the electrolyte solution of the S_v-ZIS photocatalyst is 1/9 mL. R is 8.314 J mol⁻¹ K⁻¹, F is 96485 C mol⁻¹, and the temperatures of the hot and cold sides are 315.4 and 298.6 K. The contribution of H⁺ to the thermopower in the O_v-WO₃/TGC/S_v-ZIS system is -1.9 mV K⁻¹.

When $n=1$, the thermopower of our system can be expressed as:

$$S_e = 2.7 + 0.3x \quad (26)$$

when $n=2$, the thermopower of our system can be expressed as:

$$S_e = 2.7 + 0.3x + 9 \times 10^{-6} x^2 \quad (27)$$

when $n=3$, the thermopower of our system can be expressed as:

$$S_e = 2.7 + 0.3x + 9 \times 10^{-6} x^2 + 15 \times 10^{-9} x^3 \quad (28)$$

The curves of Eqs. 26, 27, and 28 approximately conformed to the original Eqs. 20 and 21 in **Fig. S22**.

Thus, it is reasonable to simplify the analysis to $n=1$.

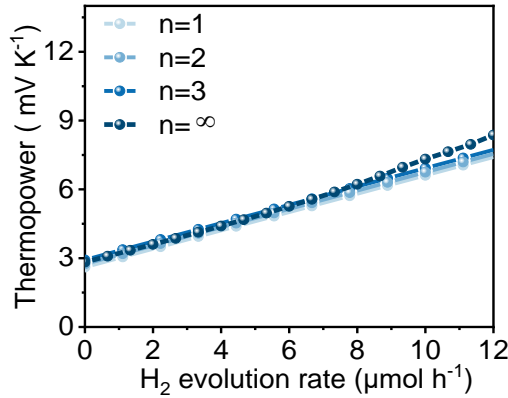


Fig. S22. The curves of theoretical function in our system for $n=1, 2, 3$, and ∞ .

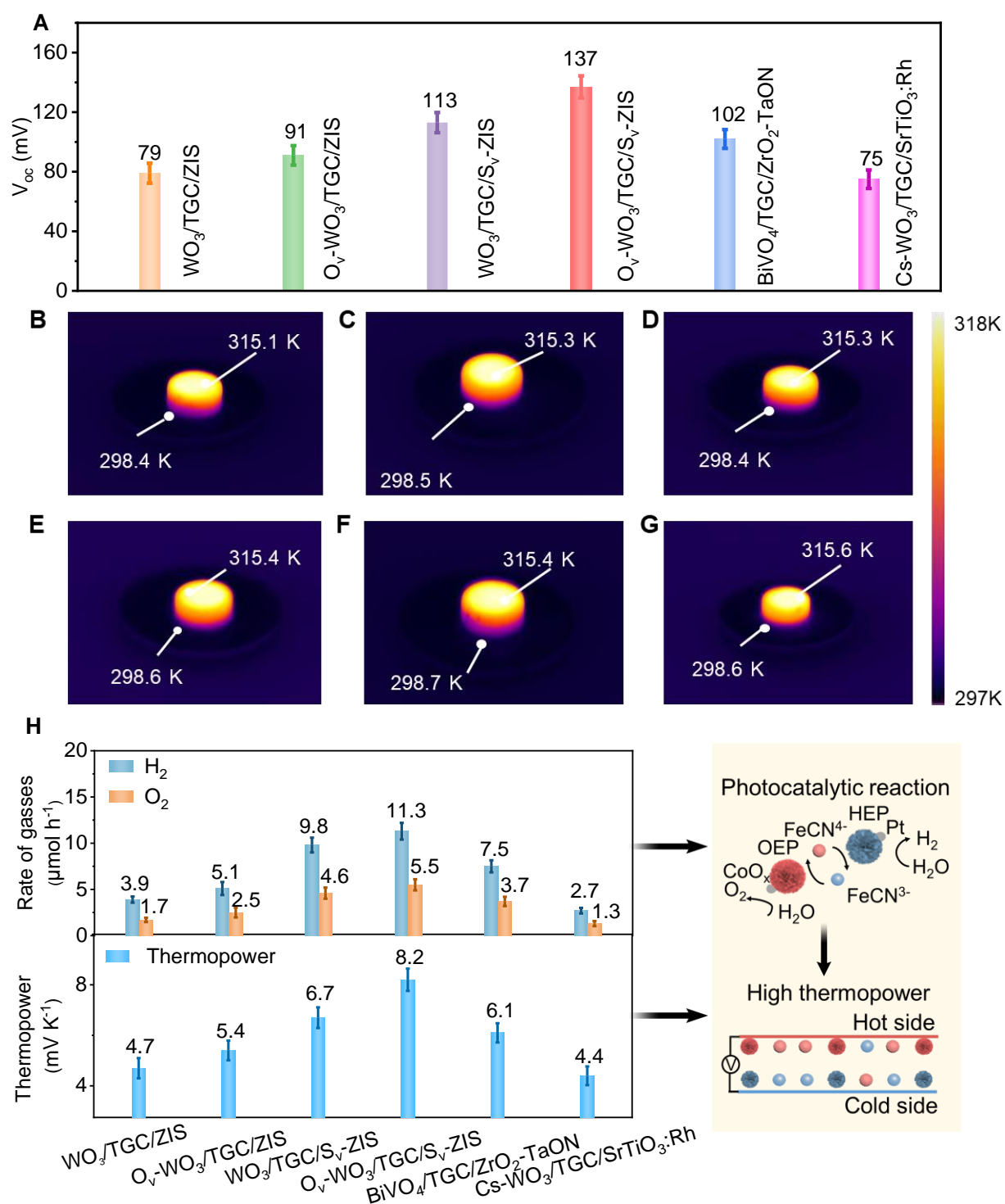


Fig. S23. The universal feature of photocatalytically enhanced thermogalvanic cells. (A) V_{oc} of the TGC system with different photocatalysts. Infrared thermal images of (B) WO₃/TGC/ZIS, (C) O_v-WO₃/TGC/ZIS, (D) WO₃/TGC/S_v-ZIS, (E) O_v-WO₃/TGC/S_v-ZIS, (F) BiVO₄/TGC/ZrO₂-TaON, and (G) Cs-WO₃/TGC/SrTiO₃:Rh, respectively. (H) Gas evolution rates (H₂ and O₂) and thermopowers in the TGC system with different photocatalysts under light irradiation. Error bars indicated the standard deviation for ten measurements.

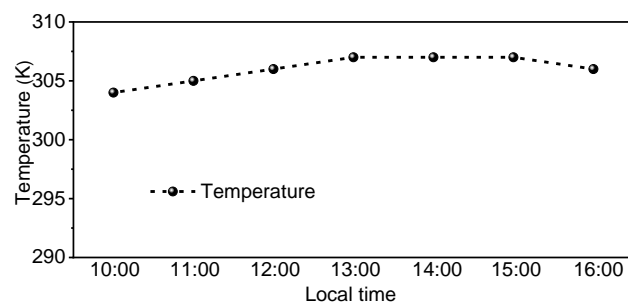


Fig. S24. The temperature profile from 10:00 to 16:00 (July 07, 2022) at Northwestern Polytechnical University of Xi'an.

Table S1. The thermopower values of system calculated based on Method one and Method two.

Method	S_e (mV K ⁻¹)	$S_{\Delta D} + S_{\Delta S}^{\text{FeCN}^{4-/3-}}$ (mV K ⁻¹)	$S_{\Delta C}^{\text{FeCN}^{4-/3-}}$ (mV K ⁻¹)	$S_{\Delta S}^{\text{H}^+} + S_{\Delta C}^{\text{H}^+}$ (mV K ⁻¹)
One	/	/	/	-1.9
Two	8.2	3.5	6.5	-1.8

Table S2. Comparison of the thermopower (S_e), $P_{\max}/(\Delta T)^2$, ZT , and η_r of this work with those reported for thermogalvanic cells in the literature.

Matrix	Redox couple	S_e (mV K ⁻¹)	$P_{\max}/(\Delta T)^2$ (mW K ⁻² m ⁻²)	ZT^*	η_r (%)	Ref.
O _v -WO ₃ /PAA/S _v -ZIS	FeCN ^{4-/3-}	8.2	8.5	0.17	4.91	This work
PAA	FeCN ^{4-/3-}	2.7	0.82	0.017	0.47	This work
tetramethylene sulfone	Fe ^{3+/2+}	2.49	0.02			(28)
polyvinyl alcohol/gelation	Fe ^{3+/2+}	1.63	0.03	0.002		(29)
PAA-carboxymethylcellulose	FeCN ^{4-/3-}	1.3	0.0325			(15)
polyvinyl alcohol	Fe ^{3+/2+}	0.79	0.05	0.0004		(30)
α -cyclodextrin	I ^{3-/2-}	2.0	0.052	0.005		(16)
H ₂ O	Co ^{3+/2+}	1.6	0.06		0.087	(31)
polyvinyl alcohol	Fe ^{3+/2+}	2.02	0.1	0.0028		(19)
H ₂ O	FeCN ^{4-/3-}	1.45	0.12			(32)
polyvinyl alcohol	FeCN ^{4-/3-}	1.5	0.17	0.01		(9)
H ₂ O	FeCN ^{4-/3-}	1.43	0.2	0.015	0.275	(33)
H ₂ O	FeCN ^{4-/3-}	1.3	0.36	0.02	0.7	(34)
H ₂ O	Fe ^{3+/2+}	1.70	0.48			(35)
H ₂ O	FeCN ^{4-/3-}	1.4	0.5		1.4	(36)
H ₂ O	Fe ^{3+/2+}	1.72	0.56			(37)
H ₂ O	FeCN ^{4-/3-}	1.43	0.6	0.014	0.4	(38)
polyacrylamide	FeCN ^{4-/3-}	1.5	0.61	0.09	1.38	(18)
H ₂ O	FeCN ^{4-/3-}	2.9	0.64	0.07	1.38	(8)
polyacrylamide	Fe ^{3+/2+}	2.91	0.66	0.002		(39)
H ₂ O	Cu/Cu ²⁺	1.66	0.71			(40)
H ₂ O	FeCN ^{4-/3-}	4.2	1.1			(2)
PAA-sodium alginate	FeCN ^{4-/3-}	4.4	1.78	0.01	3.05	(41)
H ₂ O	FeCN ^{4-/3-}	1.42	1.9		2.4	(42)
H ₂ O	FeCN ^{4-/3-}	3.73	7.08	0.4	11.1	(1)

* We calculated ZT values using the provided equation for references that contained relevant parameters. For literature that did not offer relevant parameters, we could not calculate the ZT values.

Table S3. Calculated STH values of 5 separated O_v-WO₃/TGC/S_v-ZIS samples for overall photocatalytic water splitting.

Sample	H ₂ evolution rates (μmol h ⁻¹)	O ₂ evolution rates (μmol h ⁻¹)	STH (%)
1	3.9	1.9	0.40
2	4.0	1.9	0.41
3	3.7	1.8	0.38
4	3.8	1.8	0.39
5	4.1	2.0	0.42

Using sample 1 measurement as the example, STH was estimated using Eq. 6.

$$\begin{aligned}
 \text{STH}(\%) &= \frac{R_{\text{H}_2} \Delta G_r}{\text{PS}} \times 100 \\
 &= \frac{3.9 \times 10^{-6} \times 237130}{100 \times 10^{-3} \times 0.64 \times 3600} \times 100 \\
 &= 0.40
 \end{aligned}$$

Table S4. The comparison of photocatalytic performance for overall water splitting over reported representative photocatalytic water splitting systems with aqueous redox mediators.

Catalysts	Cocatalyst	Electron mediator	Gas evolution rates ($\mu\text{mol h}^{-1}$)	STH (%)	Ref.
O _v -WO ₃ /TGC/ S _v -ZIS	Pt, CoO _x	FeCN ^{4-/3-}	H ₂ : 11.3 O ₂ : 5.5	0.4	This work
SrTiO ₃ -WO ₃	Ru	FeCN ^{4-/3-}	H ₂ : 6.05 O ₂ : 3.01	0.04	(43)
ZrO ₂ -TaON/BiVO ₄	Au, CoO _x	FeCN ^{4-/3-}	H ₂ : 105 O ₂ : 52	0.5	(24)
MgTa ₂ O _{6-x} N _y /TaON/ BiVO ₄	FeCoO _x	FeCN ^{4-/3-}	H ₂ : 160 O ₂ : 80	0.6	(23)
P10/BiVO ₄	Pd	Fe ^{3+/2+}	H ₂ : 1.0 O ₂ : 0.5	0.0014%	(55)
MOF	Pt	Fe ^{3+/2+}	H ₂ : 11.6 O ₂ : 5.8	/	(56)
BaTaO ₂ N/WO ₃	Pt, PtO _x	I ^{3-/2-}	H ₂ : 30 O ₂ : 15	0.24	(26)
HCa ₂ Nb ₃ O ₁₀ /WO ₃	Pt, PtO _x	I ^{3-/2-}	H ₂ : 11.5 O ₂ : 5.3	0.12	(57)
SrTiO ₃ :Rh/ Ru-H ₂ WO ₄	Pt, Ru	IO ₃ ⁻ /I ⁻	H ₂ : 2 O ₂ : 1	/	(58)
Ru/SrTiO ₃ :Rh/ BiVO ₄	Rh/Cr ₂ O ₃ , CoOOH	Co(bpy) ₃ ^{3+/2+}	H ₂ : 100 O ₂ : 47	0.06	(59)

Movie S1.

Demonstration of the large-area (112 cm²) photocatalytically enhanced thermogalvanic generator module induced an output of approximately 4.4 V under natural sunlight.

References and Notes

1. B. Yu, J. Duan, H. Cong, W. Xie, R. Liu, X. Zhuang, H. Wang, B. Qi, M. Xu, Z. L. Wang, J. Zhou, Thermosensitive crystallization-boosted liquid thermocells for low-grade heat harvesting. *Science* **370**, 342–346 (2020). [doi:10.1126/science.abd6749](https://doi.org/10.1126/science.abd6749) [Medline](#)
2. J. Duan, G. Feng, B. Yu, J. Li, M. Chen, P. Yang, J. Feng, K. Liu, J. Zhou, Aqueous thermogalvanic cells with a high Seebeck coefficient for low-grade heat harvest. *Nat. Commun.* **9**, 5146–5153 (2018). [doi:10.1038/s41467-018-07625-9](https://doi.org/10.1038/s41467-018-07625-9) [Medline](#)
3. K. Chen, B. Song, N. K. Ravichandran, Q. Zheng, X. Chen, H. Lee, H. Sun, S. Li, G. A. G. Udalamatta Gamage, F. Tian, Z. Ding, Q. Song, A. Rai, H. Wu, P. Koirala, A. J. Schmidt, K. Watanabe, B. Lv, Z. Ren, L. Shi, D. G. Cahill, T. Taniguchi, D. Broido, G. Chen, Ultrahigh thermal conductivity in isotope-enriched cubic boron nitride. *Science* **367**, 555–559 (2020). [doi:10.1126/science.aaz6149](https://doi.org/10.1126/science.aaz6149) [Medline](#)
4. S. Ohno, K. Imasato, S. Anand, H. Tamaki, S. D. Kang, P. Gorai, H. K. Sato, E. S. Toberer, T. Kanno, G. J. Snyder, Phase boundary mapping to obtain n-type Mg_3Sb_2 -based thermoelectrics. *Joule* **2**, 141–154 (2018). [doi:10.1016/j.joule.2017.11.005](https://doi.org/10.1016/j.joule.2017.11.005)
5. H. Wang, W. Xie, B. Yu, B. Qi, R. Liu, X. Zhuang, S. Liu, P. Liu, J. Duan, J. Zhou, Simultaneous solar steam and electricity generation from synergistic salinity-temperature gradient. *Adv. Energy Mater.* **11**, 2100481–2100486 (2021). [doi:10.1002/aenm.202100481](https://doi.org/10.1002/aenm.202100481)
6. D. Kraemer, Q. Jie, K. McEnaney, F. Cao, W. Liu, L. A. Weinstein, J. Loomis, Z. Ren, G. Chen, Concentrating solar thermoelectric generators with a peak efficiency of 7.4%. *Nat. Energy* **1**, 16153–16160 (2016). [doi:10.1038/nenergy.2016.153](https://doi.org/10.1038/nenergy.2016.153)
7. Y. Li, Q. Li, X. Zhang, B. Deng, C. Han, W. Liu, W. Liu, 3D hierarchical electrodes boosting ultrahigh power output for gelatin-KCl- $\text{FeCN}^{4-/3-}$ ionic thermoelectric cells. *Adv. Energy Mater.* **12**, 2103666–2103675 (2022). [doi:10.1002/aenm.202103666](https://doi.org/10.1002/aenm.202103666)
8. T. Kim, J. S. Lee, G. Lee, H. Yoon, J. Yoon, T. J. Kang, Y. H. Kim, High thermopower of ferri/ferrocyanide redox couple in organic-water solutions. *Nano Energy* **31**, 160–167 (2017). [doi:10.1016/j.nanoen.2016.11.014](https://doi.org/10.1016/j.nanoen.2016.11.014)
9. W. Gao, Z. Lei, W. Chen, Y. Chen, Hierarchically anisotropic networks to decouple mechanical and ionic properties for high-performance quasi-solid thermocells. *ACS Nano* **16**, 8347–8357 (2022). [doi:10.1021/acsnano.2c02606](https://doi.org/10.1021/acsnano.2c02606) [Medline](#)
10. Y. Liu, M. Cui, W. Ling, L. Cheng, H. Lei, W. Li, Y. Huang, Thermo-electrochemical cells for heat to electricity conversion: From mechanisms, materials, strategies to applications. *Energy Environ. Sci.* **15**, 3670–3687 (2022). [doi:10.1039/D2EE01457B](https://doi.org/10.1039/D2EE01457B)
11. Y. Zheng, T. J. Slade, L. Hu, X. Y. Tan, Y. Luo, Z.-Z. Luo, J. Xu, Q. Yan, M. G. Kanatzidis, Defect engineering in thermoelectric materials: What have we learned? *Chem. Soc. Rev.* **50**, 9022–9054 (2021). [doi:10.1039/D1CS00347J](https://doi.org/10.1039/D1CS00347J) [Medline](#)

12. C. G. Han, X. Qian, Q. Li, B. Deng, Y. Zhu, Z. Han, W. Zhang, W. Wang, S. P. Feng, G. Chen, W. Liu, Giant thermopower of ionic gelatin near room temperature. *Science* **368**, 1091–1098 (2020). [doi:10.1126/science.aaz5045](https://doi.org/10.1126/science.aaz5045) [Medline](#)
13. T. Li, X. Zhang, S. D. Lacey, R. Mi, X. Zhao, F. Jiang, J. Song, Z. Liu, G. Chen, J. Dai, Y. Yao, S. Das, R. Yang, R. M. Briber, L. Hu, Cellulose ionic conductors with high differential thermal voltage for low-grade heat harvesting. *Nat. Mater.* **18**, 608–613 (2019). [doi:10.1038/s41563-019-0315-6](https://doi.org/10.1038/s41563-019-0315-6) [Medline](#)
14. Y. Han, J. Zhang, R. Hu, D. Xu, High-thermopower polarized electrolytes enabled by methylcellulose for low-grade heat harvesting. *Sci. Adv.* **8**, eabl5318 (2022). [doi:10.1126/sciadv.abl5318](https://doi.org/10.1126/sciadv.abl5318) [Medline](#)
15. J. Shen, Y. Ma, C. Yang, S. Liu, J. Li, Z. Chen, B. Tian, S. Li, Boosting solar-thermal-electric conversion of thermoelectrochemical cells by construction of a carboxymethylcellulose-interpenetrated polyacrylamide network. *J. Mater. Chem. A Mater. Energy Sustain.* **10**, 7785–7791 (2022). [doi:10.1039/D2TA00025C](https://doi.org/10.1039/D2TA00025C)
16. H. Zhou, T. Yamada, N. Kimizuka, Supramolecular thermo-electrochemical cells: Enhanced thermoelectric performance by host-guest complexation and salt-induced crystallization. *J. Am. Chem. Soc.* **138**, 10502–10507 (2016). [doi:10.1021/jacs.6b04923](https://doi.org/10.1021/jacs.6b04923) [Medline](#)
17. M. Li, M. Hong, M. Dargusch, J. Zou, Z.-G. Chen, High-efficiency thermocells driven by thermo-electrochemical processes. *Trends Chem.* **3**, 561–574 (2021). [doi:10.1016/j.trechm.2020.11.001](https://doi.org/10.1016/j.trechm.2020.11.001)
18. Z. Lei, W. Gao, P. Wu, Double-network thermocells with extraordinary toughness and boosted power density for continuous heat harvesting. *Joule* **5**, 2211–2222 (2021). [doi:10.1016/j.joule.2021.06.003](https://doi.org/10.1016/j.joule.2021.06.003)
19. W. Gao, Z. Lei, C. Zhang, X. Liu, Y. Chen, Stretchable and freeze-tolerant organohydrogel thermocells with enhanced thermoelectric performance continually working at subzero temperatures. *Adv. Funct. Mater.* **31**, 2104071–2104078 (2021). [doi:10.1002/adfm.202104071](https://doi.org/10.1002/adfm.202104071)
20. T. Ding, Y. Zhou, X. Q. Wang, C. Zhang, T. Li, Y. Cheng, W. Lu, J. He, G. W. Ho, All-soft and stretchable thermogalvanic gel fabric for antideformity body heat harvesting wearable. *Adv. Energy Mater.* **11**, 2102219–2102227 (2021). [doi:10.1002/aenm.202102219](https://doi.org/10.1002/aenm.202102219)
21. Y. Liu, H. Wang, P. C. Sherrell, L. Liu, Y. Wang, J. Chen, Potentially wearable thermo-electrochemical cells for body heat harvesting: From mechanism, materials, strategies to applications. *Adv. Sci. (Weinh.)* **8**, 2100669–2100681 (2021). [doi:10.1002/advs.202100669](https://doi.org/10.1002/advs.202100669)
22. Y. Liu, S. Zhang, Y. Zhou, M. A. Buckingham, L. Aldous, P. C. Sherrell, G. G. Wallace, G. Ryder, S. Faisal, D. L. Officer, S. Beirne, J. Chen, Advanced wearable thermocells for body heat harvesting. *Adv. Energy Mater.* **10**, 2002539–2002548 (2020). [doi:10.1002/aenm.202002539](https://doi.org/10.1002/aenm.202002539)

23. Y. Qi, J. Zhang, Y. Kong, Y. Zhao, S. Chen, D. Li, W. Liu, Y. Chen, T. Xie, J. Cui, C. Li, K. Domen, F. Zhang, Unraveling of cocatalysts photodeposited selectively on facets of BiVO₄ to boost solar water splitting. *Nat. Commun.* **13**, 484–492 (2022). [doi:10.1038/s41467-022-28146-6](https://doi.org/10.1038/s41467-022-28146-6) [Medline](#)
24. Y. Qi, Y. Zhao, Y. Gao, D. Li, Z. Li, F. Zhang, C. Li, Redox-based visible-light-driven Z-scheme overall water splitting with apparent quantum efficiency exceeding 10%. *Joule* **2**, 2393–2402 (2018). [doi:10.1016/j.joule.2018.07.029](https://doi.org/10.1016/j.joule.2018.07.029)
25. Y. Wang, W. Huang, S. Guo, X. Xin, Y. Zhang, P. Guo, S. Tang, X. Li, Sulfur-deficient ZnIn₂S₄/oxygen-deficient WO₃ hybrids with carbon layer bridges as a novel photothermal/photocatalytic integrated system for Z-scheme overall water splitting. *Adv. Energy Mater.* **11**, 2102452–2102460 (2021). [doi:10.1002/aenm.202102452](https://doi.org/10.1002/aenm.202102452)
26. Z. Wang, Y. Luo, T. Hisatomi, J. J. M. Vequizo, S. Suzuki, S. Chen, M. Nakabayashi, L. Lin, Z. Pan, N. Kariya, A. Yamakata, N. Shibata, T. Takata, K. Teshima, K. Domen, Sequential cocatalyst decoration on BaTaO₂N towards highly-active Z-scheme water splitting. *Nat. Commun.* **12**, 1005–1013 (2021). [doi:10.1038/s41467-021-21284-3](https://doi.org/10.1038/s41467-021-21284-3) [Medline](#)
27. S. Guo, Y. Li, S. Tang, Y. Zhang, X. Li, A. J. Sobrido, M. M. Titirici, B. Wei, Monitoring hydrogen evolution reaction intermediates of transition metal dichalcogenides via operando raman spectroscopy. *Adv. Funct. Mater.* **30**, 2003035–2003043 (2020). [doi:10.1002/adfm.202003035](https://doi.org/10.1002/adfm.202003035)
28. Y. Liu, Q. Zhang, G. O. Odunmbaku, Y. He, Y. Zheng, S. Chen, Y. Zhou, J. Li, M. Li, K. Sun, Solvent effect on the seebeck coefficient of Fe²⁺/Fe³⁺ hydrogel thermogalvanic cells. *J. Mater. Chem. A Mater. Energy Sustain.* **10**, 19690–19698 (2022). [doi:10.1039/D1TA10508F](https://doi.org/10.1039/D1TA10508F)
29. C. Bai, X. Li, X. Cui, X. Yang, X. Zhang, K. Yang, T. Wang, H. Zhang, Transparent stretchable thermogalvanic PVA/gelation hydrogel electrolyte for harnessing solar energy enabled by a binary solvent strategy. *Nano Energy* **100**, 107449–107457 (2022). [doi:10.1016/j.nanoen.2022.107449](https://doi.org/10.1016/j.nanoen.2022.107449)
30. C. Bai, Z. Wang, S. Yang, X. Cui, X. Li, Y. Yin, M. Zhang, T. Wang, S. Sang, W. Zhang, H. Zhang, Wearable electronics based on the gel thermogalvanic electrolyte for self-powered human health monitoring. *ACS Appl. Mater. Interfaces* **13**, 37316–37322 (2021). [doi:10.1021/acsami.1c12443](https://doi.org/10.1021/acsami.1c12443) [Medline](#)
31. P. F. Salazar, S. T. Stephens, A. H. Kazim, J. M. Pringle, B. A. Cola, Enhanced thermo-electrochemical power using carbon nanotube additives in ionic liquid redox electrolytes. *J. Mater. Chem. A Mater. Energy Sustain.* **2**, 20676–20682 (2014). [doi:10.1039/C4TA04749D](https://doi.org/10.1039/C4TA04749D)
32. Y. Yang, S. W. Lee, H. Ghasemi, J. Loomis, X. Li, D. Kraemer, G. Zheng, Y. Cui, G. Chen, Charging-free electrochemical system for harvesting low-grade thermal energy. *Proc. Natl. Acad. Sci. U.S.A.* **111**, 17011–17016 (2014). [doi:10.1073/pnas.1415097111](https://doi.org/10.1073/pnas.1415097111) [Medline](#)
33. T. J. Kang, S. Fang, M. E. Kozlov, C. S. Haines, N. Li, Y. H. Kim, Y. Chen, R. H. Baughman, Electrical power from nanotube and graphene electrochemical thermal energy harvesters. *Adv. Funct. Mater.* **22**, 477–489 (2012). [doi:10.1002/adfm.201101639](https://doi.org/10.1002/adfm.201101639)

34. G. Li, D. Dong, G. Hong, L. Yan, X. Zhang, W. Song, High-efficiency cryo-thermocells assembled with anisotropic holey graphene aerogel electrodes and a eutectic redox electrolyte. *Adv. Mater.* **31**, e1901403 (2019). [doi:10.1002/adma.201901403](https://doi.org/10.1002/adma.201901403) [Medline](#)
35. J. H. Kim, T. J. Kang, Diffusion and current generation in porous electrodes for thermo-electrochemical cells. *ACS Appl. Mater. Interfaces* **11**, 28894–28899 (2019). [doi:10.1021/acsami.9b08381](https://doi.org/10.1021/acsami.9b08381) [Medline](#)
36. R. Hu, B. A. Cola, N. Haram, J. N. Barisci, S. Lee, S. Stoughton, G. Wallace, C. Too, M. Thomas, A. Gestos, M. E. Cruz, J. P. Ferraris, A. A. Zakhidov, R. H. Baughman, Harvesting waste thermal energy using a carbon-nanotube-based thermo-electrochemical cell. *Nano Lett.* **10**, 838–846 (2010). [doi:10.1021/nl903267n](https://doi.org/10.1021/nl903267n) [Medline](#)
37. J. H. Lee, G. Shin, J. Y. Baek, T. J. Kang, An electricity-generating window made of a transparent energy harvester of thermocells. *ACS Appl. Mater. Interfaces* **13**, 21157–21165 (2021). [doi:10.1021/acsami.1c00164](https://doi.org/10.1021/acsami.1c00164) [Medline](#)
38. L. Zhang, T. Kim, N. Li, T. J. Kang, J. Chen, J. M. Pringle, M. Zhang, A. H. Kazim, S. Fang, C. Haines, D. Al-Masri, B. A. Cola, J. M. Razal, J. Di, S. Beirne, D. R. MacFarlane, A. Gonzalez-Martin, S. Mathew, Y. H. Kim, G. Wallace, R. H. Baughman, High power density electrochemical thermocells for inexpensively harvesting low-grade thermal energy. *Adv. Mater.* **29**, 1605652–1605658 (2017). [doi:10.1002/adma.201605652](https://doi.org/10.1002/adma.201605652) [Medline](#)
39. C. Xu, Y. Sun, J. Zhang, W. Xu, H. Tian, Adaptable and wearable thermocell based on stretchable hydrogel for body heat harvesting. *Adv. Energy Mater.* **12**, 2201542 (2022). [doi:10.1002/aenm.202201542](https://doi.org/10.1002/aenm.202201542)
40. B. Yu, H. Xiao, Y. Zeng, S. Liu, D. Wu, P. Liu, J. Guo, W. Xie, J. Duan, J. Zhou, Cost-effective n-type thermocells enabled by thermosensitive crystallizations and 3D multi-structured electrodes. *Nano Energy* **93**, 106795–106803 (2022). [doi:10.1016/j.nanoen.2021.106795](https://doi.org/10.1016/j.nanoen.2021.106795)
41. D. Zhang, Y. Mao, F. Ye, Q. Li, P. Bai, W. He, R. Ma, Stretchable thermogalvanic hydrogel thermocell with record-high specific output power density enabled by ion-induced crystallization. *Energy Environ. Sci.* **15**, 2974–2982 (2022). [doi:10.1039/D2EE00738J](https://doi.org/10.1039/D2EE00738J)
42. M. S. Romano, N. Li, D. Antiohos, J. M. Razal, A. Nattestad, S. Beirne, S. Fang, Y. Chen, R. Jalili, G. G. Wallace, R. Baughman, J. Chen, Carbon nanotube - reduced graphene oxide composites for thermal energy harvesting applications. *Adv. Mater.* **25**, 6602–6606 (2013). [doi:10.1002/adma.201303295](https://doi.org/10.1002/adma.201303295) [Medline](#)
43. Y. Miseki, K. Sayama, Photocatalytic water splitting employing a $[\text{Fe}(\text{CN})_6]^{3-/4-}$ redox mediator under visible light. *Catal. Sci. Technol.* **9**, 2019–2024 (2019). [doi:10.1039/C9CY00100J](https://doi.org/10.1039/C9CY00100J)
44. D. Zhao, Y. Wang, C.-L. Dong, Y.-C. Huang, J. Chen, F. Xue, S. Shen, L. Guo, Boron-doped nitrogen-deficient carbon nitride-based Z-scheme heterostructures for photocatalytic overall water splitting. *Nat. Energy* **6**, 388–397 (2021). [doi:10.1038/s41560-021-00795-9](https://doi.org/10.1038/s41560-021-00795-9)

45. G. Kresse, J. Furthmüller, Efficient iterative schemes for ab initio total-energy calculations using a plane-wave basis set. *Phys. Rev. B Condens. Matter* **54**, 11169–11186 (1996). [doi:10.1103/PhysRevB.54.11169](https://doi.org/10.1103/PhysRevB.54.11169) [Medline](#)
46. J. P. Perdew, K. Burke, M. Ernzerhof, K. B. John P. Perdew, Matthias Ernzerhof, Generalized gradient approximation made simple. *Phys. Rev. Lett.* **77**, 3865–3868 (1996). [doi:10.1103/PhysRevLett.77.3865](https://doi.org/10.1103/PhysRevLett.77.3865) [Medline](#)
47. H. J. Monkhorst, J. D. Pack, Special points for Brillouin-zone integrations. *Phys. Rev. B* **13**, 5188–5192 (1976). [doi:10.1103/PhysRevB.13.5188](https://doi.org/10.1103/PhysRevB.13.5188)
48. S. Grimme, J. Antony, S. Ehrlich, H. Krieg, A consistent and accurate ab initio parametrization of density functional dispersion correction (DFT-D) for the 94 elements H-Pu. *J. Chem. Phys.* **132**, 154104–154121 (2010). [doi:10.1063/1.3382344](https://doi.org/10.1063/1.3382344) [Medline](#)
49. K. Mathew, R. Sundararaman, K. Letchworth-Weaver, T. A. Arias, R. G. Hennig, Implicit solvation model for density-functional study of nanocrystal surfaces and reaction pathways. *J. Chem. Phys.* **140**, 084106–084113 (2014). [doi:10.1063/1.4865107](https://doi.org/10.1063/1.4865107) [Medline](#)
50. J. R. J. K. Nørskov, A. Logadottir, L. Lindqvist, Origin of the overpotential for oxygen reduction at a fuel-cell cathode. *J. Phys. Chem. B* **108**, 17886–17892 (2004). [doi:10.1021/jp047349j](https://doi.org/10.1021/jp047349j)
51. Z. Sun, R. Huo, C. Choi, S. Hong, T.-S. Wu, J. Qiu, C. Yan, Z. Han, Y. Liu, Y.-L. Soo, Y. Jung, Oxygen vacancy enables electrochemical N₂ fixation over WO₃ with tailored structure. *Nano Energy* **62**, 869–875 (2019). [doi:10.1016/j.nanoen.2019.06.019](https://doi.org/10.1016/j.nanoen.2019.06.019)
52. X. Wang, X. Wang, J. Huang, S. Li, A. Meng, Z. Li, Interfacial chemical bond and internal electric field modulated Z-scheme S_v-ZnIn₂S₄/MoSe₂ photocatalyst for efficient hydrogen evolution. *Nat. Commun.* **12**, 4112–4122 (2021). [doi:10.1038/s41467-021-24511-z](https://doi.org/10.1038/s41467-021-24511-z) [Medline](#)
53. Y. Zhao, C. Ding, J. Zhu, W. Qin, X. Tao, F. Fan, R. Li, C. Li, A hydrogen farm strategy for scalable solar hydrogen production with particulate photocatalysts. *Angew. Chem. Int. Ed.* **59**, 9653–9658 (2020). [doi:10.1002/anie.202001438](https://doi.org/10.1002/anie.202001438) [Medline](#)
54. X. Zheng, L. Feng, Y. Dou, H. Guo, Y. Liang, G. Li, J. He, P. Liu, J. He, High carrier separation efficiency in morphology-controlled BiOBr/C schottky junctions for photocatalytic overall water splitting. *ACS Nano* **15**, 13209–13219 (2021). [doi:10.1021/acsnano.1c02884](https://doi.org/10.1021/acsnano.1c02884)
55. Y. Bai, K. Nakagawa, A. J. Cowan, C. M. Aitchison, Y. Yamaguchi, M. A. Zwijnenburg, A. Kudo, R. S. Sprick, A. I. Cooper, Photocatalyst Z-scheme system composed of a linear conjugated polymer and BiVO₄ for overall water splitting under visible light. *J. Mater. Chem. A Mater. Energy Sustain.* **8**, 16283–16290 (2020). [doi:10.1039/D0TA04754F](https://doi.org/10.1039/D0TA04754F)
56. H. Hu, Z. Wang, L. Cao, L. Zeng, C. Zhang, W. Lin, C. Wang, Metal-organic frameworks embedded in a liposome facilitate overall photocatalytic water splitting. *Nat. Chem.* **13**, 358–366 (2021). [doi:10.1038/s41557-020-00635-5](https://doi.org/10.1038/s41557-020-00635-5) [Medline](#)
57. S. Nishioka, K. Hojo, L. Xiao, T. Gao, Y. Miseki, S. Yasuda, T. Yokoi, K. Sayama, T. E. Mallouk, K. Maeda, Surface-modified, dye-sensitized niobate nanosheets enabling an

efficient solar-driven Z-scheme for overall water splitting. *Sci. Adv.* **8**, eadc9115 (2022).
[doi:10.1126/sciadv.adc9115](https://doi.org/10.1126/sciadv.adc9115) [Medline](#)

58. H. Suzuki, S. Nitta, O. Tomita, M. Higashi, R. Abe, Highly dispersed RuO₂ hydrates prepared via simple adsorption as efficient cocatalysts for visible-light-driven z-scheme water splitting with an IO₃⁻/I⁻ redox mediator. *ACS Catal.* **7**, 4336–4343 (2017).
[doi:10.1021/acscatal.7b00953](https://doi.org/10.1021/acscatal.7b00953)
59. Y. Sasaki, H. Kato, A. Kudo, [Co(bpy)₃]^{3+/2+} and [Co(phen)₃]^{3+/2+} electron mediators for overall water splitting under sunlight irradiation using Z-scheme photocatalyst system. *J. Am. Chem. Soc.* **135**, 5441–5449 (2013). [doi:10.1021/ja400238r](https://doi.org/10.1021/ja400238r) [Medline](#)